

## A fast computational model for near-and far-field noise prediction due to offshore pile driving

Peng, Yaxi; Tsouvalas, Apostolos; Stampoultzoglou, Tasos; Metrikine, Andrei

**DOI**

[10.1121/10.0003752](https://doi.org/10.1121/10.0003752)

**Publication date**

2021

**Document Version**

Final published version

**Published in**

Journal of the Acoustical Society of America

**Citation (APA)**

Peng, Y., Tsouvalas, A., Stampoultzoglou, T., & Metrikine, A. (2021). A fast computational model for near-and far-field noise prediction due to offshore pile driving. *Journal of the Acoustical Society of America*, 149(3), 1772-1790. <https://doi.org/10.1121/10.0003752>

**Important note**

To cite this publication, please use the final published version (if applicable). Please check the document version above.

**Copyright**

Other than for strictly personal use, it is not permitted to download, forward or distribute the text or part of it, without the consent of the author(s) and/or copyright holder(s), unless the work is under an open content license such as Creative Commons.

**Takedown policy**

Please contact us and provide details if you believe this document breaches copyrights. We will remove access to the work immediately and investigate your claim.

# A fast computational model for near- and far-field noise prediction due to offshore pile driving

Yaxi Peng, Apostolos Tsouvalas, Tasos Stampoultzoglou, and Andrei Metrikine

Citation: [The Journal of the Acoustical Society of America](#) **149**, 1772 (2021); doi: 10.1121/10.0003752

View online: <https://doi.org/10.1121/10.0003752>

View Table of Contents: <https://asa.scitation.org/toc/jas/149/3>

Published by the [Acoustical Society of America](#)

---

## ARTICLES YOU MAY BE INTERESTED IN

[Validation of a finite element modelling approach for mitigated and unmitigated pile driving noise prognosis](#)  
The Journal of the Acoustical Society of America **149**, 1737 (2021); <https://doi.org/10.1121/10.0003756>

[Allan Pierce and adiabatic normal modes](#)

The Journal of the Acoustical Society of America **149**, R5 (2021); <https://doi.org/10.1121/10.0003595>

[Detection of envelope modulation and direction of arrival estimation of multiple noise sources with an acoustic vector sensor](#)

The Journal of the Acoustical Society of America **149**, 1596 (2021); <https://doi.org/10.1121/10.0003628>

[Multichannel deconvolution of vibrational signals: A state-space inverse filtering approach](#)

The Journal of the Acoustical Society of America **149**, 1749 (2021); <https://doi.org/10.1121/10.0003750>

[Shape optimization of acoustic horns for improved directivity control and radiation efficiency based on the multimodal method](#)

The Journal of the Acoustical Society of America **149**, 1411 (2021); <https://doi.org/10.1121/10.0003568>

[A one-dimensional flow model enhanced by machine learning for simulation of vocal fold vibration](#)

The Journal of the Acoustical Society of America **149**, 1712 (2021); <https://doi.org/10.1121/10.0003561>

---



Advance your science and career  
as a member of the

ACOUSTICAL SOCIETY OF AMERICA

LEARN MORE



## A fast computational model for near- and far-field noise prediction due to offshore pile driving

Yaxi Peng,<sup>1,a)</sup> Apostolos Tsouvalas,<sup>1,b),c)</sup> Tasos Stampoulzoglou,<sup>2</sup> and Andrei Metrikine<sup>1,b),d)</sup>

<sup>1</sup>Department of Structural Engineering, Delft University of Technology, Stevinweg 1, 2628CN, Delft, Netherlands

<sup>2</sup>Department of Engineering and Estimating Offshore/Offshore Wind, Van Oord, Schaardijk 211, 3063NH, Rotterdam, Netherlands

### ABSTRACT:

This paper presents a computationally efficient modeling approach for predicting underwater noise radiation from offshore pile driving. The complete noise prediction model comprises two modules. First, a sound generation module is adopted to capture the interaction between the pile, the fluid, and the seabed, aiming at modeling the sound generation and propagation in the vicinity of the pile. Second, a sound propagation module is developed to propagate the sound field at larger distances from the pile. To couple the input wavefield obtained from the sound generation module, the boundary integral equations (BIEs) are formulated based on the acousto-elastodynamic reciprocity theorem. To advance the mathematical formulation of the BIEs, the Green's tensor for an axisymmetric ring load is derived using the complex wavenumber integration technique. The model advances the computational efficiency and flexibility of the noise prediction in both near- and far-fields from the pile. Finally, model predictions are benchmarked against a theoretical scenario and validated using measurement data from a recent offshore pile-installation campaign. © 2021 Acoustical Society of America. <https://doi.org/10.1121/10.0003752>

(Received 15 October 2020; revised 17 February 2021; accepted 21 February 2021; published online 12 March 2021)

[Editor: Nicole Kessissoglou]

Pages: 1772–1790

### I. INTRODUCTION

Underwater noise generated by offshore pile driving has raised serious concerns over the ecological impact on marine life (Bailey *et al.*, 2010). In recent years, a large number of offshore wind farms have been built, which intensifies the negative effect induced by impact pile driving (Hastie *et al.*, 2019). Recent studies have shown that the emission of the high-intensity impulsive noise not only leads to temporary habitat loss for porpoises and dolphins but also increases the risk of causing temporary or permanent hearing damage of those marine mammals (Ainslie *et al.*, 2020; Hastie *et al.*, 2019). To preserve the marine ecosystem and maintain sustainable development, strict governmental regulations are being imposed targeting the threshold levels of underwater noise (Rossington *et al.*, 2013). Therefore, an environmental impact assessment that includes the prediction of noise levels is required prior to the construction of the installation of piles in most projects (Stöber and Thomsen, 2019). Given the expected noise levels, appropriate noise mitigation systems (NMS), i.e., bubble curtains, hydro-sound damper, or noise mitigation screen, are usually required to reduce the noise (Verfuß, 2014).

Over the last few decades, modeling the underwater noise generated by offshore pile driving has been studied extensively with various computational methods (Tsouvalas,

2020). In most available models, a two-step modeling approach is adopted. A sound generation model, based on either finite elements (FEs) (Reinhall and Dahl, 2011; Zampolli *et al.*, 2013) or finite differences (MacGillivray, 2014), is employed for sound generation purposes. Subsequently, a sound propagation model is used to propagate sound at larger distances based on the normal mode method (Wilkes and Gavrilov, 2017; Wilkes *et al.*, 2016), the wavenumber integration method (Lippert and von Estorff, 2014), or the parabolic equation method (Kim *et al.*, 2012). Reinhall and Dahl (Reinhall and Dahl, 2011) were the first to examine systematically the noise generated by the impact pile driving. Using FE simulations, they have shown that the sound waves in the seawater region originate from the radial expansion of the pile surface caused by the compressional waves traveling the pile downward at supersonic speed, the latter radiating waves in the water in the form of Mach cones. A complete physics-based noise prediction model, including modeling the soil as an elastic medium in the near-field and modeling of an impact hammer, was proposed by Fricke and Rolfes (2015). The modeled results agree well with noise measurement data, which confirm the validity of the model and reveal that the main damping mechanism for the pile vibration is the radiation of shear waves into the soil and not frictional sliding between the pile and soil. Based on the conceptualization of the radiated sound field as an array of moving point sources, several simplified models reproduced the sound field from pile driving by employing the wavenumber integration technique (Lippert and Lippert, 2012) or the parabolic equation method (Dahl and Dall'Osto, 2017; Reinhall and Dahl,

<sup>a)</sup>Electronic mail: y.peng@tudelft.nl

<sup>b)</sup>Also at: Department of Hydraulic Engineering, Delft University of Technology, Stevinweg 1, 2628CN, Delft, Netherlands.

<sup>c)</sup>ORCID: 0000-0002-5830-5654.

<sup>d)</sup>ORCID: 0000-0002-3514-3541.

2011). The results were generally found to be in good qualitative agreement with those of more detailed FE simulations. Lippert and von Estorff (2014) presented a coupled FE and wavenumber integration model and investigated the influence of uncertainties of sediment parameters through Monte-Carlo simulations. The numerical predictions by the different models are basically consistent with each other (Lippert and von Estorff, 2014). With only a few exceptions (Fricke and Rolfes, 2015), the seabed is customarily approximated by an equivalent acoustic fluid with extra attenuation. However, it is well-known that the pile-driving sources located in the seafloor are not purely compressional in nature but emit both compressional and shear waves (Hazelwood and Macey, 2016; Hazelwood *et al.*, 2018; Nealy *et al.*, 2016). A detailed description of the soil is essential to correctly capture the noise source characteristics (pile vibrations). The influence of the pile inclination and three-dimensional effects are examined by recent models (von Pein *et al.*, 2019; Wilkes and Gavrilov, 2017), which are applicable for raked piles and vertically positioned piles driven in range and angular-dependent environments.

In contrast to the models above, several semi-analytical models were also developed to predict underwater noise from pile driving (Deng *et al.*, 2016a; Deng *et al.*, 2016b; Hall, 2013, 2015; Tsouvalas and Metrikine, 2013, 2014). The model developed by Tsouvalas and Metrikine (2013) describes adequately the most critical components of the system, i.e., the hydraulic hammer, the pile, and the water, while the seabed is described by linear springs and dashpots, which account for soil elasticity and energy absorption, respectively. This paper aims to capture primarily the pile dynamics and near-field noise prediction, but not very close to the seabed surface. Subsequently, a more complete pile-water-soil interaction model was developed by Tsouvalas and Metrikine (2014), which additionally included a three-dimensional description of the water-saturated seabed as a layered elastic medium. In that work (Tsouvalas and Metrikine, 2014), the significance of the seabed-water interface waves (Scholte waves) was also investigated for the first time; the model predictions were later confirmed by collected measurement data (Tsouvalas and Metrikine, 2016). Although Scholte waves travel at relatively low wave speed and attenuate quickly, they need to be accounted for in the sound generation model in order to accurately describe the pile vibrations and energy distribution in the domain of interest (Tsouvalas *et al.*, 2015). The primary noise transmission path is in the water column in the form of Mach cones, while the secondary noise path is attributed primarily to Scholte waves, which propagate along the seabed-water interface (Hazelwood and Macey, 2016; Hazelwood *et al.*, 2018). Examining these two noise transmission paths is key to the effective blockage of the noise propagation by exploiting the proper functioning of noise mitigation systems. Similar to the semi-analytical model (Tsouvalas and Metrikine, 2013), the model proposed by Deng *et al.* (2016a) focused on examining the influence of the non-axisymmetric impact loading and the interaction of the anvil

and the pile. Next to the semi-analytical models discussed above, a damped cylindrical spreading (DCS) model was developed by Lippert *et al.* (2018), which estimates the sound exposure level (SEL) due to impact piling using an analytical approach. Similarly, a linear mixed model additionally takes into account the influence of the variability in the sound propagation (Martin and Barclay, 2019) and later is extended with the regression analysis for acoustic impact criteria (Ainslie *et al.*, 2020).

Given the discussion above, most available models are either detailed, i.e., FE models coupled to the propagation models, or simplified empirical ones. While the former ones are accurate but computationally slow, the latter are fast but cannot accurately predict the noise field, especially when NMS are deployed. In the near-field, detailed FE models including the elastic description of the seabed can encounter numerical issues for higher frequencies as the limit of the perfect matched layer, including angle-dependent absorption and heavy computation due to the very fine mesh size required to account for the shear waves. Next to that, the semi-analytical models discussed are valid for predictions in the vicinity of the pile but not valid at a larger horizontal distance from the pile due to the introduction of the artificial boundary at a large depth to accommodate the mode-matching solution approach (Tsouvalas and Metrikine, 2014), which will cause artificial reflection of the waves. The primary purpose of this paper is to present a computationally efficient method for the prediction of the generation and propagation of the sound field associated with impact piling at large (from the pile) distances, overcoming the limitations of earlier models. The complete model consists of two modules: (i) a sound generation module aiming at the accurate description of the pile-water-soil interaction together with the sound emission in the vicinity of the pile and (ii) a sound propagation module aiming at the propagation of the wavefield at larger distances with high accuracy.

The main contribution of the present model is that it advances the accuracy, computational efficiency, and flexibility of the noise prediction in both near- and far-fields. First, the sound generation module captures the vibroacoustic behavior of the coupled pile-water-soil system. It provides an accurate description of the input wavefield in terms of both stresses and displacements at the pile proximity. This field is subsequently fed into the sound propagation module. The complex wavenumber integration technique adopted in the latter advances the mathematical treatment of the Green's function for an acousto-elastic layered half-space. The choice of the branch cut ensures both stability and convergence of the obtained solution. The attenuation in multilayered soil half-space is included by identifying the exact poles and branch cuts in the complex wavenumber plane, which is especially important for noise predictions up to a few kilometers. The accuracy of the model predictions is demonstrated against measurement data up to 1500 m from the pile. Apart from the pressure waves in the water column and compressional and shear waves in the seabed, the Scholte and Stoneley waves at the water-soil and soil-

soil interfaces are captured in both modules. Second, compared to the classical FE models coupled to the propagation models, the model presented herein is computationally more efficient and can be used in probabilistic analysis of noise prediction involving a large number of simulations with less computational effort. Compared to the equivalent fluid-based, far-range sound propagation model, the sound propagation module is computationally fast and provides a more detailed description of the elastic seabed. Third, the eigenproblems of the shell and the surrounding acousto-elastic medium can be solved independently, which provides great flexibility in examining various configurations of the system. The response of the pile and the acousto-elastic medium can then be derived for the coupled problem using the given modal sets and the mode-matching method, which greatly reduce the computation time. The present model allows an in-depth analysis of water- and soil-borne noise transmission paths independently and can be used for the prediction of noise reduction level by combining it with various modeling techniques, i.e., air bubble curtain system, hydro-sound damper system, and underwater Helmholtz resonators.

The structure of this paper is as follows. In Sec. II, the governing equations and model description are presented. In Secs. III and IV, the solution method is presented as a two-step approach consisting of the sound generation module and the sound propagation module. In Sec. V, the numerical evaluation of the solutions is presented based on the normal mode solution with complex wavenumber integration addressing both numerical stability and convergence. The choice of the branch cuts and the physical interpretation of contributions from discrete poles are also discussed. In Sec. VI, the solution is validated against results obtained by FE simulations. Section VII is dedicated to a numerical analysis

of several benchmark cases, which proves the validity of the model for the prediction of underwater noise from offshore pile driving. Finally, the conclusions are given in Sec. VIII.

## II. MODEL DESCRIPTION AND GOVERNING EQUATIONS

In this section, the description of the model and the governing equations of the fully coupled vibroacoustic system are introduced. The geometry and material properties of the system are given first, followed by the equations of motion of the vibrating shell, the fluid, and the soil together with the boundary and interface conditions. Finally, a schematic overview of the computational method is presented.

### A. Description of the model

The total system consists of the pile structure, the hydraulic hammer, and the surrounding fluid and soil media as shown in Fig. 1 (left). A symmetric cylindrical coordinate system  $(r, \phi, z)$  is introduced for the fluid and soil domain with the depth  $z$  being positive downward and  $r$  being the radial distance from the  $z$  axis. The model is assumed to be range-independent. The displacement field is described as  $u_\xi = [u_\xi, \theta_\xi, w_\xi]$  with  $\xi = f$  or  $j$  indicating the fluid layer or soil layer  $j$ . Because of axial symmetry, the displacement in the  $\phi$ -direction  $\theta_\xi$  is trivially zero. Based on the assumption that the fluid and the soil inside the pile do not significantly influence the vibration of the pile and the radiated energy in the surrounding medium (Tsouvalas and Metrikine, 2013), the water column and the soil inside the pile are not included in this model. The complete model consists of two modules, a sound generation module and a sound propagation module. The sound generation module comprises the pile modeled as a linear elastic thin shell and the surrounding media

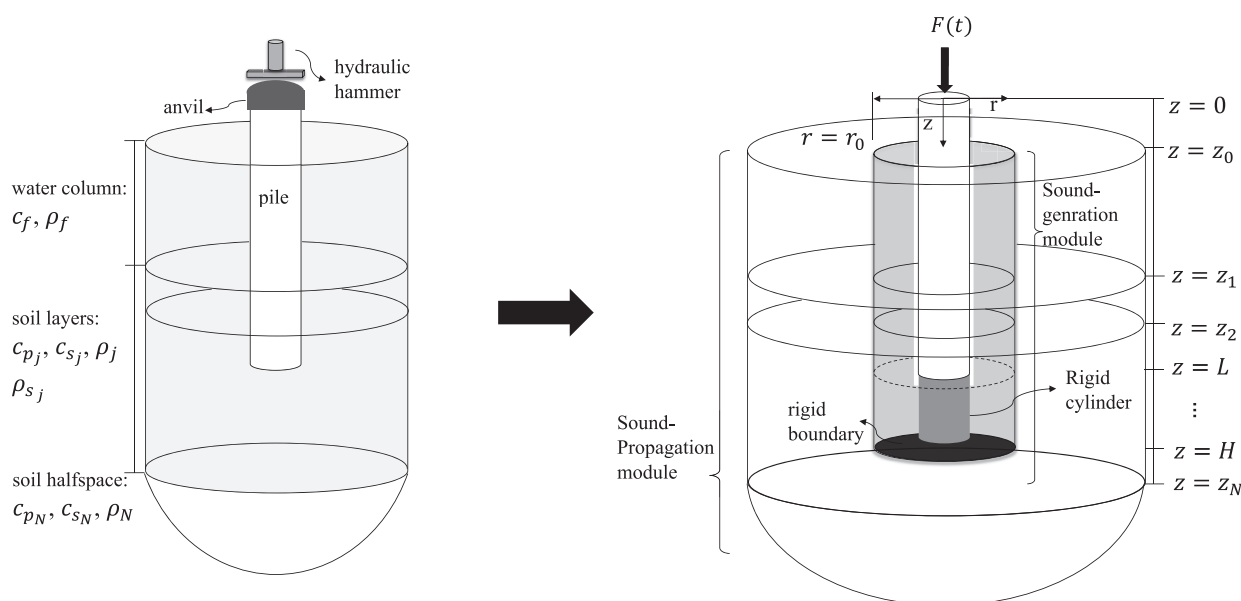


FIG. 1. Schematic of the complete system (left) and the coupled model (right):  $r_0$  is the radial distance of the coupled cylindrical surface;  $z_0$  is the level of the sea surface;  $z_1$  is the level of the seabed;  $z_j$  is the bottom level of the  $j - 1$ th soil layer ( $j = 2, 3 \dots N$ );  $L$  indicates the level of the bottom of pile tip;  $H$  indicates the level of the rigid boundary applied in the sound generation module.

modeled as a horizontally stratified acousto-elastic waveguide (Tsouvalas, 2015; Tsouvalas and Metrikine, 2014). A rigid cylinder of the same radius as the pile and of height  $H-L$  is placed below the pile tip, which allows one to employ the semi-analytical solution adopted in this work. By doing so, the radiation of elastic waves from the tip of the pile into the deeper soil layers is omitted. However, this assumption is not expected to influence the noise predictions and the elastic wave propagation in the shallow soil layers close to the seafloor. The hydraulic hammer and anvil are not modeled explicitly but substituted by an external force exerted at the top of the pile ( $z=0$ ). The forcing function is obtained from available measurement data or numerical models (Fricke and Rolfes, 2015; Zampolli et al., 2013). The dynamic response of the shell structure is described by a linear high-order shell theory (Kaplunov et al., 1998). The high-order shell theory is chosen to accommodate all combinations of pile sizes and excitation frequencies, as the high-order approximations are more accurate at higher frequency bands and do not involve any extra computational cost in the solution approach adopted in this paper (Kaplunov et al., 1998; Tsouvalas, 2015). The pile occupies the domain  $0 \leq z \leq L$ , with the material and geometrical constants  $E$ ,  $\nu$ ,  $R$ ,  $\rho$ , and  $t$  being the complex modulus of elasticity in the frequency domain, the Poisson ratio, the radius of the mid-surface of the shell, and the density and thickness of the shell, respectively. In both modules, the fluid is modeled as a three-dimensional inviscid compressible medium with constants  $c_f$  and  $\rho_f$  being the wave speed and the density of the fluid, which occupies the domain  $z_0 \leq z \leq z_1$  with  $R \leq r \leq r_0$  for the sound generation module and  $r \geq r_0$  for the sound propagation module. The soil is modeled as a three-dimensional elastic continuum occupying the domain  $z \geq z_1$ . The constants  $\lambda_j$ ,  $\mu_j$ , and  $\rho_j$  correspond to the Lamé coefficients and the density of the solid, with the index  $j = 1, 2, \dots, N$  specifying the soil layers including the bottom soil half-space. The material dissipation (damping) in the soil is introduced in the form of complex Lamé constants  $\tilde{\lambda}_j$  and  $\tilde{\mu}_j$  as  $\tilde{\lambda}_j = \lambda_j \cdot (1 + i \cdot \alpha_{1j})$  and  $\tilde{\mu}_j = \mu_j \cdot (1 + i \cdot \alpha_{2j})$ . The attenuation coefficients  $\alpha_{1j}$  and  $\alpha_{2j}$  are defined as  $(20\pi \log_{10} e)\alpha_{p_j}$  and  $(20\pi \log_{10} e)\alpha_{s_j}$ , respectively, with  $\alpha_{p_j}$  and  $\alpha_{s_j}$  being the compressional and shear damping coefficients in units of dB per wavelength.

**B. Governing equations**

The following partial differential equations govern the dynamic response of coupled system consisting of the shell structure and the acousto-elastic media in the time domain:

$$\mathbf{L}\mathbf{u} + \mathbf{I}\ddot{\mathbf{u}} = -(H(z - z_1) - H(z - L))\mathbf{t}_s + (H(z - z_0) - H(z - z_1))\mathbf{p}_f + \mathbf{f}_e, \tag{1}$$

$$\nabla^2 p_f(r, z, t) - \frac{1}{c_f^2} \ddot{p}_f(r, z, t) = 0, \tag{2}$$

$$(\lambda_j + 2\mu_j)\nabla(\nabla \cdot \mathbf{u}_j) - \mu_j \nabla \times (\nabla \times \mathbf{u}_j) = \rho_j \ddot{\mathbf{u}}_j. \tag{3}$$

In Eq. (1),  $\mathbf{u} = [u_z(z, t) \ u_r(z, t)]^T$  is the displacement vector of the mid-surface of the shell with  $0 < z < L$ . The operators  $\mathbf{L}$  and  $\mathbf{I}$  are the stiffness and modified inertia matrices of the shell, respectively (Tsouvalas and Metrikine, 2014). The term  $\mathbf{t}_s$  represents the boundary stress vector that takes into account the reaction of the soil surrounding the shell  $z_1 \leq z \leq L$ . The term  $\mathbf{p}_f$  represents the fluid pressure exerted at the outer surface of the shell at  $z_0 \leq z \leq z_1$ . The functions  $H(z - z_i)$  are the Heaviside step functions. The vector  $\mathbf{f}_e = [f_z(z, t) \ f_r(z, t)]^T$  represents the externally applied force on the surface of the shell. In Eq. (2),  $p_f(r, z, t)$  is the pressure field of the fluid. In Eq. (3),  $\mathbf{u}_j = [w_j(r, z, t) \ u_j(r, z, t)]^T$  is the vertical and radial displacements of soil layer  $j$ .

The Helmholtz decomposition can be applied to the fluid-soil domain as

$$\mathbf{u}_f = \nabla \phi_f, \quad \mathbf{u}_j = \nabla \phi_j + \nabla \times \left( 0, -\frac{\partial \psi_j}{\partial r}, 0 \right). \tag{4}$$

Substitution of Eq. (4) into Eqs. (2) and (3) yields (Ewing et al., 1957)

$$\nabla^2 \phi_f(r, z, t) = \frac{1}{c_f^2} \frac{\partial^2 \phi_f}{\partial t^2}, \tag{5}$$

$$\nabla^2 \phi_j(r, z, t) = \frac{1}{c_{p_j}^2} \frac{\partial^2 \phi_j}{\partial t^2}, \tag{6}$$

$$\nabla^2 \psi_j(r, z, t) = \frac{1}{c_{s_j}^2} \frac{\partial^2 \psi_j}{\partial t^2}. \tag{7}$$

In the equations above,  $c_{p_j}$  and  $c_{s_j}$  denote the speeds of the compressional and shear waves in soil layer  $j$ , respectively.

The pressure release boundary condition is applied at the sea surface. At the fluid-soil interface  $z = z_1$ , the vertical stress equilibrium and the vertical displacement continuity are imposed, while the shear stress vanishes, since no tangential stresses present in a perfect fluid. For the sound generation module, the interface at  $z = H$  is substituted by a rigid boundary at a great depth, whereas the bottom soil is extended to infinity to mimic realistic ocean environments in the sound propagation module. In the following examined cases,  $H = z_N$ . The choice of the  $z_N$  ( $z_N \geq H$ ) for practical cases is related to the depth of the soil layer, which is determined by the soil profiles provided by the offshore geotechnical survey. The rigid cylinder below the pile is not expected to have a significant influence on the energy distributions and the resulting pressure level in the fluid. This assumption is confirmed in the sequel by direct comparison with the measured data. To minimize the effect of the artificial reflection from the rigid boundary, the sound generation module is coupled to the sound propagation module at a very close distance to the pile surface, so the influence of the rigid boundary becomes insignificant.

Given the full-contact at the soil-soil interface, both stress equilibrium and displacement continuity are applied. This set of boundary and interface conditions reads

$$p_f(r, z_0, t) = 0, \quad r \geq R, \tag{8}$$

$$\begin{aligned} \sigma_{zz_1}(r, z_1, t) + p_f(r, z_1, t) &= 0, \\ u_{z,f}(r, z_1, t) &= w_{s1}(r, z_1, t), \quad \sigma_{zr_1}(r, z_1, t) = 0, \\ r &\geq R, \end{aligned} \tag{9}$$

$$\begin{aligned} w_j(r, z_j, t) &= w_{j-1}(r, z_j, t), \\ u_j(r, z_j, t) &= u_{j-1}(r, z_j, t), \quad 2 \leq j \leq N, \quad r \geq R, \end{aligned} \tag{10}$$

$$\begin{aligned} \sigma_{zz_j}(r, z_j, t) &= \sigma_{zz_{j-1}}(r, z_j, t), \\ \sigma_{zr_j}(r, z_j, t) &= \sigma_{zr_{j-1}}(r, z_j, t), \\ 2 \leq j &\leq N, \quad r \geq R. \end{aligned} \tag{11}$$

In Eq. (11),  $\sigma_{zz_j}$  and  $\sigma_{zr_j}$  designate the normal and tangential stresses in the soil layer  $j$ . For  $r < r_0$ , a rigid surface is placed at  $z = H$  (in the sound generation module) as depicted in Fig. 1 (right). At the pile-water interface, the pressure equilibrium and displacement continuity are imposed. Under the assumption of no pile slip, a perfect contact condition is applied at the pile-soil interface. The set of kinematic conditions at the interface of the shell and the surrounding media ( $r = R$ ) are given as

$$\begin{aligned} u_r(z, t) &= u_f(R, z, t), \quad z_0 \leq z \leq z_1, \\ u_r(z, t) &= u_j(R, z, t) \quad \text{and} \quad u_z(z, t) = w_j(R, z, t), \\ z_1 \leq z &\leq L, \quad 1 \leq j \leq N. \end{aligned} \tag{12}$$

After applying the forward Fourier transform, the governing equations in frequency domain are obtained. The Fourier transform pair used in this paper is expressed as

$$\begin{aligned} g(t) &= \frac{1}{2\pi} \int_{-\infty}^{+\infty} \tilde{G}(\omega) e^{-i\omega t} d\omega \\ \text{and} \quad \tilde{G}(\omega) &= \int_{-\infty}^{+\infty} g(t) e^{i\omega t} dt, \end{aligned} \tag{13}$$

in which  $g(t)$  and  $\tilde{G}(\omega)$  denote the physical quantities in the time and frequency domains, respectively.

### C. An overview of the computational method

The diagram of the complete model is shown in Fig. 2, which presents the computational method of the model and the process of the simulation. As indicated in the diagram, variation of a certain input parameter, e.g., the penetration depth of the pile or the input forcing function, requires solely part of the simulation to be recomputed, which significantly improves the computation efficiency of the model for running a large number of parametric analysis.

### III. SOUND GENERATION MODULE

The sound generation module is based on a three-dimensional cylindrically symmetric vibroacoustic model developed by Tsouvalas and Metrikine (2014). The module captures the dynamic interactions between the pile and the surrounding media. A modal decomposition is applied to

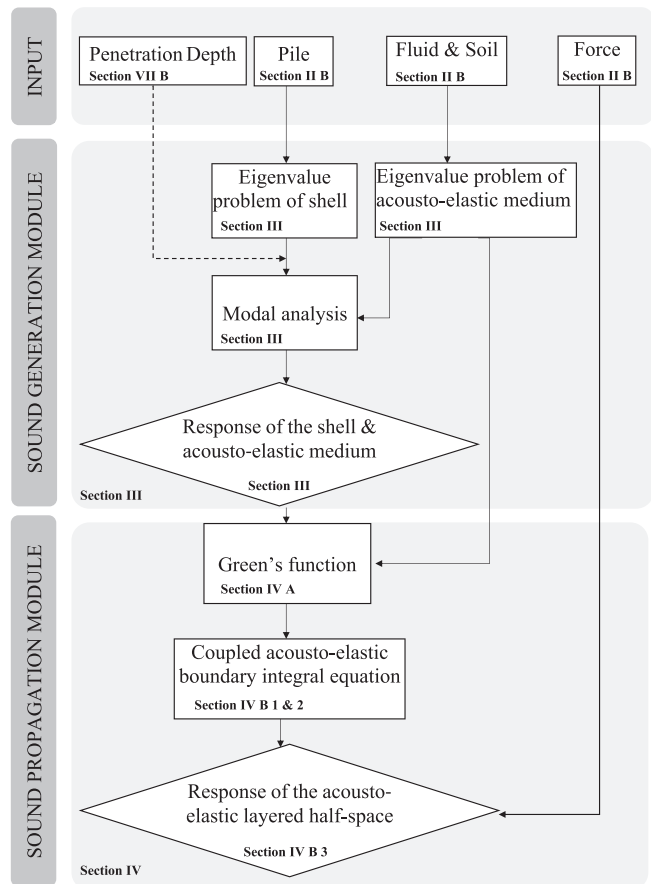


FIG. 2. Diagram of the computational approach of the model and its components.

both the shell structure and the acousto-elastic waveguide. Based on the mode-matching technique, the response of a coupled pile-water-soil system is obtained in the frequency domain. The wavenumber spectrum associated with the evanescent waves of the waveguide is significant for the vibroacoustic interaction problem as shown in Tsouvalas *et al.* (2015). A set of the response functions in terms of pressure, velocity, displacement, and stress tensors is obtained as input for the sound propagation model discussed in Sec. IV. The expressions for the fluid pressure are given in Tsouvalas and Metrikine (2014) as follows:

$$\tilde{p}_f(r, z, \omega) = \sum_{p=1}^{\infty} C_p H_0^{(2)}(k_p r) \tilde{p}_{f,p}(z), \tag{14}$$

in which the complex-valued coefficients  $C_p$  are determined by solving the forced response of the complete coupled system, and  $\tilde{p}_{f,p}(z)$  are the eigenfunction of the pressure for the mode  $p$ . The expressions for velocities in the fluid, displacement, and stresses in the soil can be found in Eqs. (40)–(44) in Tsouvalas and Metrikine (2014).

Because the complete system is linear and the eigenvalue problems of the shell and the acousto-elastic waveguide are solved independently, only part of the simulation is required for a large number of predictions with various

inputs. The sound generation module allows various scenarios (i.e., various forcing functions, soil conditions, penetration depths, etc.) to be investigated with significantly less computational effort compared to the FE or finite-difference models, since only part of the simulation needs to be evaluated when input parameters are varied.

IV. SOUND PROPAGATION MODULE

The input to the sound propagation module is provided by the sound generation module through a boundary integral formulation (Achenbach, 1973; Beskos, 1987; Jensen et al., 2011). This section comprises two parts. Section IV A describes the derivation of the Green’s functions, whereas Sec. IV B discusses the formulation of the boundary integrals.

A. Green’s functions

A solution of the wave equation in acousto-elastic ocean environments was first developed by Press and Ewing (1950). They extended the Pekeris theory of normal mode model from two liquid layers into the case of a fluid layer overlying a solid bottom. The solution presented by Press and Ewing is an approximation that holds for observation points at large radial positions solely, which renders the branch line integrals insignificant. Schmidt and Jensen (1985) dealt with the case of a multilayered viscoelastic medium and employed the wavenumber integration approach to tackle the problem similarly to Ewing et al. (1957). The solution for Green’s function by Nealy et al. (2016) generalizes the previous approaches by considering a point source in the elastic seabed or on the acousto-elastic interface. Bakr (1986) applies the boundary integral equation (BIE) methods in the analysis of the axisymmetric acoustic and elastic problem. The Green’s function for a ring source is presented for infinite acoustic domain or elastic domain. In this paper, the solution of Green’s functions for ring load in acousto-elastic half-space is derived, and the boundary integral formulation is extended for the coupled acousto-elastic case.

To propagate the axisymmetric wavefield generated by the sound generation module, Green’s tensors for a fluid layer overlying a multilayered soil half-space are first derived for an arbitrary source excitation. The Hankel transform and complex contour integration approach are used to obtain a closed-form response in the frequency domain. The Hankel transform pair is given as (Abramowitz and Stegun, 1964)

$$\hat{f}(k_r) = \int_0^\infty f(r)J_0(k_r r)rdr$$

$$\text{and } f(r) = \int_0^\infty \hat{f}(k_r)J_0(k_r r)k_r dk_r, \tag{15}$$

in which  $f(r)$  and  $\hat{f}(k_r)$  denote the functions in the frequency domain and Hankel domain, respectively.  $J_0(k_r r)$  is the Bessel function of the first kind of order zero, and  $k_r$  is the horizontal wavenumber of the medium.

1. Fluid source

To derive the Green’s functions for an acoustic source, a pressure-type ring source is placed at  $[r_s, z_s]$  in the fluid domain, which generates pressure waves and produces a unit pressure amplitude at the location of the source. The equation of motion for the displacement potential reads

$$\left[\nabla^2 + k_f^2\right]\tilde{\phi}_{f,f}^g(r, z; r_s, z_s, \omega)$$

$$= \frac{1}{-\rho\omega^2} \frac{\delta(r - r_s, z - z_s)}{2\pi r}, \quad r_s \geq R, \quad z_0 \leq z_s \leq z_1, \tag{16}$$

in which the first subscript of the Green’s potential function denotes the location of the receiver, and the second subscript denotes the location of the source with  $f$  being the fluid domain. The homogeneous equations of motion for the displacement potentials  $\phi_{s,f}$  and  $\psi_{s,f}$  in the soil are given by Eqs. (6) and (7). Applying the forward Hankel transform to Eqs. (6), (7), and (16), the wave equations are reduced to depth-separated wave equations in the Hankel domain, for which the similar expressions can be found in Bakr (1986),

$$\left[\frac{d^2}{dz^2} + k_{z,f}^2\right]\hat{\phi}_{f,f}^g(k_r, z; r_s, z_s, \omega)$$

$$= \frac{1}{-\rho\omega^2} \delta(z - z_s) \frac{J_0(k_r r_s)}{2\pi}, \tag{17}$$

$$\left[\frac{d^2}{dz^2} + k_{z,p_j}^2\right]\hat{\phi}_{j,f}^g(k_r, z; r_s, z_s, \omega) = 0, \tag{18}$$

$$\left[\frac{d^2}{dz^2} + k_{z,s_j}^2\right]\hat{\psi}_{j,f}^g(k_r, z; r_s, z_s, \omega) = 0, \tag{19}$$

in which  $k_{z,\xi} = \sqrt{k_\xi^2 - k_r^2}$  is the vertical wavenumber in the domain  $\xi$  ( $=f, p_j$ , or  $s_j$ ). The boundary conditions of the acousto-elastic medium along the  $z$  coordinate have been specified in Eqs. (8)–(11).

The solutions for the displacement potentials are the sum of a particular solution and the general solution to the homogeneous equation:

$$\hat{\phi}_{f,f}^g(k_r, z; r_s, z_s, \omega)$$

$$= \left(\frac{1}{-\rho\omega^2} \frac{e^{-ik_{z,f}|z-z_s|}}{4\pi i k_{z,f}} + A_1^g e^{ik_{z,f}z} + A_2^g e^{-ik_{z,f}z}\right) J_0(k_r r_s), \tag{20}$$

$$\hat{\phi}_{j,f}^g(k_r, z; r_s, z_s, \omega) = (A_{4j-1}^g e^{ik_{z,p_j}z} + A_{4j}^g e^{-ik_{z,p_j}z}) J_0(k_r r_s), \tag{21}$$

$$\hat{\psi}_{j,f}^g(k_r, z; r_s, z_s, \omega) = (A_{4j+1}^g e^{ik_{z,s_j}z} + A_{4j+2}^g e^{-ik_{z,s_j}z}) J_0(k_r r_s), \tag{22}$$

in which the coefficients  $A_i^g$  ( $i = 1, 2, \dots, 4N + 2$ ) are undetermined complex amplitudes. Two unknown amplitude coefficients in the potential function  $\phi_f$  indicate upward-

and downward-propagating waves in the fluid, and four unknown amplitude coefficients in the functions  $\phi_s$  and  $\psi_s$  indicate upward- and downward-propagating waves in each soil layer. When  $j=N$ , the amplitudes in front of the first term in both Eqs. (21) and (22) vanish to ensure the radiation condition at infinity in  $z$ -direction. When deriving the Green's functions for the soil source, the soil layer containing the source is divided into two layers, above and below the soil source, to end with homogeneous equations of motion and the excitation included in the interface conditions. This introduces an extra four unknown amplitudes of  $\phi_s$  and  $\psi_s$ . Therefore, the total number of unknown amplitude coefficients is  $4N + 2$  for the fluid sources and  $4N + 6$  for the soil sources.

Applying the inverse Hankel transform with the use of the relationships of the Bessel functions (Abramowitz and Stegun, 1964), the Green's tensor of the acousto-elastic medium in the frequency domain is obtained as

$$\begin{aligned} \tilde{\Phi}_{\Xi f}^g(r, z; r_s, z_s, \omega) \\ = -\frac{1}{2} \int_{-\infty}^{+\infty} (\hat{\Phi}_{\Xi f}^g(k_r, z; r_s, z_s, \omega)) H_0^{(2)}(k_r r) k_r dk_r, \end{aligned} \quad (23)$$

in which  $\hat{\Phi}_{\Xi f}^g = [\hat{\phi}_{f,ff}^g, \hat{\phi}_{j,ff}^g, \hat{\psi}_{j,ff}^g]^T$  denotes the solutions of displacement potential functions in the Hankel domain, and  $\tilde{\Phi}_{\Xi f}^g$  are the corresponding potential functions in the frequency domain.

The pressure, displacements, and stresses of the acousto-elastic medium are expressed by the Green's functions of displacement potentials, which are omitted here for the sake of brevity (Achenbach, 1973; Ewing et al., 1957). By substituting the expressions into the boundary and interface conditions shown in Eqs. (9)–(12), the final set of linear algebraic equations with unknowns  $A_i^g$  for  $i = 1, 2, \dots, 4N + 2$  is obtained and given in the Appendix. Once the amplitude coefficients are solved for every  $k_r$ , the Green's tensor for a pressure-type ring source placed in the fluid domain is obtained.

## 2. Soil source

For a radial or vertical ring load applied in the soil as shown in Fig. 3, the corresponding jump condition is applied for the stresses at the plane of the source level  $z = z_s$ . Because all soil layers are free of body-force sources in that case, the solutions for the potential functions can be defined as

$$\hat{\phi}_{f,s_n}^g(k_r, z; r_s, z_s, \omega) = (A_1^g e^{ik_z z} + A_2^g e^{-ik_z z}) J_0(k_r r_s), \quad (24)$$

$$\hat{\phi}_{j,s_n}^g(k_r, z; r_s, z_s, \omega) = (A_{4j-1}^g e^{ik_z z} + A_{4j}^g e^{-ik_z z}) J_0(k_r r_s), \quad (25)$$

$$\hat{\psi}_{j,s_n}^g(k_r, z; r_s, z_s, \omega) = (A_{4j+1}^g e^{ik_z z} + A_{4j+2}^g e^{-ik_z z}) J_0(k_r r_s), \quad (26)$$

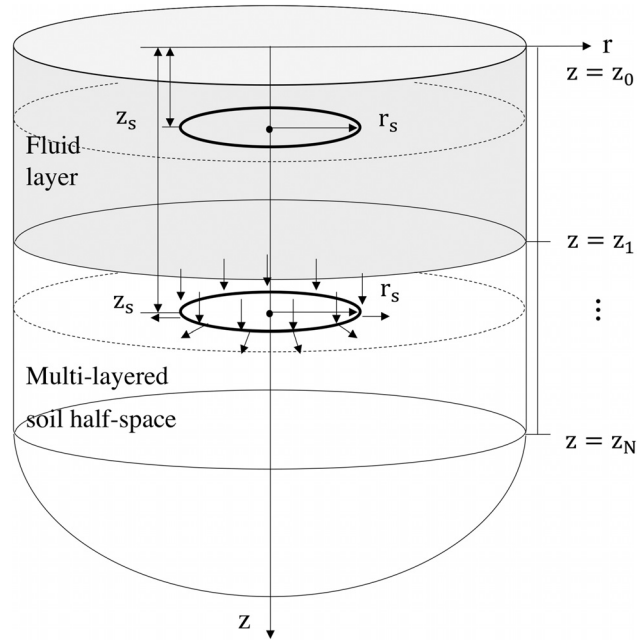


FIG. 3. Schematic of the ring source at  $r = r_s$  in the configuration of acousto-elastic layered half-space.

in which the coefficients  $A_i^g$  ( $i = 1, 2, \dots, 4N + 6$ ) are undetermined complex amplitudes, and the subscript  $n$  denotes the layer of the soil source. When  $j = n$ , the soil layer  $j$  is separated into two sublayers at  $z = z_s$ , which are denoted as  $\hat{\phi}_{s_n^+, s_n}^g$  and  $\hat{\phi}_{s_n^-, s_n}^g$  with “+” and “-” indicating the layer above and below the source level. The same notation is used for the shear potentials as  $\hat{\psi}_{s_n^+, s_n}^g$  and  $\hat{\psi}_{s_n^-, s_n}^g$ . Similar to the case of the fluid source, when  $j = N$ , the amplitudes  $A_{4j-1}^g$  and  $A_{4j+1}^g$  are set to zero to satisfy the radiation condition in  $z$ -direction.

For the radial load case, the following set of interface conditions hold at  $z = z_s$  in the Hankel domain:

$$\hat{\sigma}_{zr_{s_n^+}, s_n}^g(k_r, z_s, \omega) - \hat{\sigma}_{zr_{s_n^-}, s_n}^g(k_r, z_s, \omega) = \frac{J_0(k_r r_s)}{2\pi}, \quad (27)$$

$$\hat{\sigma}_{zz_{s_n^+}, s_n}^g(k_r, z_s, \omega) = \hat{\sigma}_{zz_{s_n^-}, s_n}^g(k_r, z_s, \omega), \quad (28)$$

$$\hat{u}_{\alpha_{s_n^+}, s_n}^g(k_r, z_s, \omega) = \hat{u}_{\alpha_{s_n^-}, s_n}^g(k_r, z_s, \omega), \quad \alpha = r, z. \quad (29)$$

Similarly, for the vertical load case, one obtains

$$\hat{\sigma}_{zz_{s_n^+}, s_n}^g(k_r, z_s, \omega) - \hat{\sigma}_{zz_{s_n^-}, s_n}^g(k_r, z_s, \omega) = \frac{J_0(k_r r_s)}{2\pi}, \quad (30)$$

$$\hat{\sigma}_{zr_{s_n^+}, s_n}^g(k_r, z_s, \omega) = \hat{\sigma}_{zr_{s_n^-}, s_n}^g(k_r, z_s, \omega), \quad (31)$$

$$\hat{u}_{\alpha_{s_n^+}, s_n}^g(k_r, z_s, \omega) = \hat{u}_{\alpha_{s_n^-}, s_n}^g(k_r, z_s, \omega), \quad \alpha = r, z. \quad (32)$$

Combining Eqs. (27)–(32) with Eqs. (8)–(11), after transformation of the latter to the Hankel domain, a linear algebraic system is formed with unknowns  $A_i^g$  for  $i = 1, 2, \dots, 4N + 6$ . Once the displacement potentials are determined in the Hankel domain, the expressions for the Green's tensors of

displacement and stress in the frequency domain can be obtained.

### 3. Closed-form response in the frequency domain

The evaluation of the integrals given by Eq. (23) can be achieved mainly in two ways: (1) by the direct wavenumber integration along with the real axis of  $k_r$ ; (2) by using the contour integration technique, i.e., by the superposition of residues of the poles enclosed by the complex integration contour and complex wavenumber integration along two branch cuts.

The second approach is basically the *normal mode* method enriched with the branch line integration as depicted in Fig. 4. The integral along the real axis can be expressed as

$$\int_{-\infty}^{+\infty} f(k_r) dk_r = -2\pi i \sum_{m=1}^M \text{Res}(k_r^{(m)}) + \int_{\alpha+\beta} \quad (33)$$

in which  $\text{Res}(f(k_r), k_r^{(m)})$  is the residue of a general function  $f(k_r)$  to a simple pole at  $k_r = k_r^{(m)}$ .

By applying the complex contour integration technique, the expressions of displacement potential functions in the frequency domain are given as a summation over a finite number of poles supplemented by the Ewing–Jardetsky–Press (EJP) branch line integrations, i.e.,

$$\begin{aligned} \tilde{\Phi}_{\Xi, \xi}^g(r, z; r_s, z_s; \omega) &= -\pi i \sum_{m=1}^M \left[ \text{Res}(\hat{\Phi}_{\Xi, \xi}^g(k_r^{(m)}, z; r_s, z_s)) H_0^{(2)}(k_r^{(m)} r) k_r^{(m)} \right] \\ &+ \frac{1}{2} \int_{\alpha+\beta} \hat{\Phi}_{\Xi, \xi}^g(k_r, z; r_s, z_s) H_0^{(2)}(k_r r) k_r dk_r. \end{aligned} \quad (34)$$

In this paper, the authors adopt the normal mode solutions together with EJP (Buckingham and Giddens, 2006; Ewing et al., 1957) complex wavenumber integration to provide the exact solution for the wave field. As shown in Fig. 4, the EJP branch cuts are given in two hyperbolic lines starting from the branch points, which are the medium wavenumbers

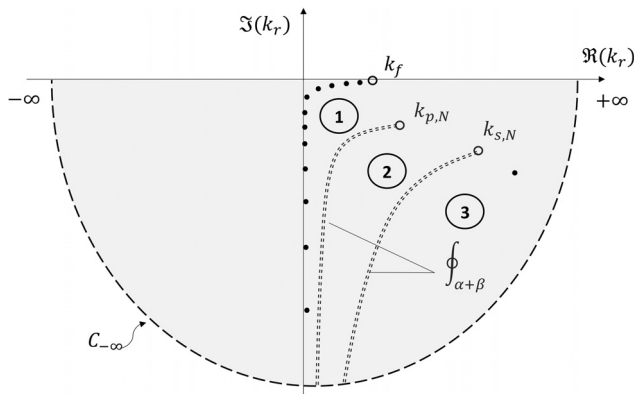


FIG. 4. Complex horizontal wavenumber  $k_r$  plane and three Riemann sheets.

corresponding to compressional and shear waves. The full solutions consist of three terms: (a) a finite sum of discrete modes on the principal Riemann surface (can be infinite in the case of the fluid layer overlying multilayered elastic half-space), in which all modes are convergent; (b) a hyperbolic branch line integration associated with the branch point of compressional wavenumber  $k_p$ ; (c) a hyperbolic branch line integration associated with the branch point of shear wavenumber  $k_s$ . The above solutions provide the basis of the sound propagation model.

### B. Boundary integral formulation

The direct boundary element method (BEM) is adopted to couple the sound generation and sound propagation modules. The solution of the acousto-elastic wavefield employs Somigliana’s identity in elastodynamics and Green’s third identity in potential theory (Beskos, 1987; Jensen et al., 2011). The velocity, displacement, and pressure/stresses on the cylindrical boundary surface  $r = r_s$  are obtained from the sound generation module. The Green’s functions obtained in Sec. IV A are the fundamental solutions for the BIEs.

The fundamental solutions of Green’s displacement tensors  $\tilde{U}_{\alpha\beta}^{\Xi\xi}(\mathbf{r}, \mathbf{r}_s, \omega)$  are derived from the potential functions (Achenbach, 1973), given the receiver point at  $\mathbf{r} = (r, z)$  (in medium  $\Xi$ ) in  $\alpha$ -direction due to a unit impulse at source  $\mathbf{r}_s = (r_s, z_s)$  (in medium  $\xi$ ) in  $\beta$ -direction:

$$\tilde{U}_{\alpha\beta}^{s\xi}(\mathbf{r}, \mathbf{r}_s, \omega) = \nabla \tilde{\phi}_{j,\xi}^g(\mathbf{r}, \mathbf{r}_s, \omega) + \nabla \times W, \quad (35)$$

$$\tilde{U}_{\alpha\beta}^{f\xi}(\mathbf{r}, \mathbf{r}_s, \omega) = \nabla \tilde{\phi}_{f,\xi}^g(\mathbf{r}, \mathbf{r}_s, \omega), \quad (36)$$

in which  $W = -\partial \psi_{s_j, \xi}^g(\mathbf{r}, \mathbf{r}_s, \omega) / \partial r$ . The displacement potential functions of the acousto-elastic domain have been derived in Eq. (34) in Sec. IV A. The Green’s stress tensors  $\tilde{T}_{\alpha\beta}^{\Xi\xi}(\mathbf{r}, \mathbf{r}_s, \omega)$  related to  $\tilde{U}_{\alpha\beta}^{\Xi\xi}(\mathbf{r}, \mathbf{r}_s, \omega)$  can be obtained through substitution of Eqs. (35) and (36) into the constitutive equations (Achenbach, 1973).

#### 1. Boundary integrals for sources located in the acoustic layer

Based on a set of acoustic sources in the form of pressure  $\tilde{p}_f(\mathbf{r}_s, \omega)$ , radial displacement  $\tilde{u}_f(\mathbf{r}_s, \omega)$ , and radial velocity fields  $\tilde{v}_{r_f}(\mathbf{r}_s, \omega)$  obtained from the sound generation modules on the cylindrical surface in the water column, a set of pressure, velocity, and displacement expressions reads

$$\begin{aligned} \tilde{p}_{f,f}(\mathbf{r}, \omega) &= \int_{S_f} (\tilde{p}_{f,f}^g(\mathbf{r}, \mathbf{r}_s, \omega) \tilde{u}_f(\mathbf{r}_s, \omega) \\ &- \tilde{u}_{f,f}^g(\mathbf{r}, \mathbf{r}_s, \omega) \tilde{p}_f(\mathbf{r}_s, \omega)) dS(\mathbf{r}_s), \end{aligned} \quad (37)$$

$$\begin{aligned} \tilde{v}_{\alpha f_f}(\mathbf{r}, \omega) &= \int_{S_f} \left( \tilde{v}_{\alpha f_f}^g(\mathbf{r}, \mathbf{r}_s, \omega) \frac{\tilde{v}_{r_f}(\mathbf{r}_s, \omega)}{i\omega} \right. \\ &+ \left. \frac{1}{\rho\omega^2} \frac{\partial \tilde{v}_{\alpha f_f}^g(\mathbf{r}, \mathbf{r}_s, \omega)}{\partial r} \tilde{p}_f(\mathbf{r}_s, \omega) \right) dS(\mathbf{r}_s), \end{aligned} \quad (38)$$

$\alpha = z, r,$

$$\begin{aligned} \tilde{u}_{\alpha, sf}(\mathbf{r}, \omega) = & \int_{S_f} \left( \tilde{u}_{\alpha, sf}^g(\mathbf{r}, \mathbf{r}_s, \omega) \frac{\tilde{v}_{r_f}(\mathbf{r}_s, \omega)}{i\omega} \right. \\ & \left. + \frac{1}{\rho\omega^2} \frac{\partial \tilde{u}_{\alpha, sf}^g(\mathbf{r}, \mathbf{r}_s, \omega)}{\partial r} \tilde{p}_f(\mathbf{r}_s, \omega) \right) dS(\mathbf{r}_s), \\ & \alpha = z, r, \end{aligned} \quad (39)$$

in which  $S_f$  and indicates the cylindrical integration surface in the fluid domain at  $r = r_s$ . Similarly, the stress components  $\tilde{\sigma}_{zz, sf}(\mathbf{r}, \omega)$ ,  $\tilde{\sigma}_{rr, sf}(\mathbf{r}, \omega)$ , and  $\tilde{\sigma}_{rz, sf}(\mathbf{r}, \omega)$  are obtained through the stress-displacement relationships (Bakr, 1986), in terms of the displacement components  $\tilde{u}_{\alpha, sf}$ .

### 2. Boundary integrals for sources located in the elastic layered half-space

Based on a set of soil sources in the form of stresses  $[\tilde{r}_r^n(\mathbf{r}_s, \omega), \tilde{t}_z^n(\mathbf{r}_s, \omega)]$  and displacements  $[\tilde{u}_r(\mathbf{r}_s, \omega), \tilde{u}_z(\mathbf{r}_s, \omega)]$  obtained from the sound generation modules on the cylindrical surface in the soil domain, a set of pressure, velocity, and displacement expressions reads

$$\begin{aligned} \tilde{p}_{f, s}(\mathbf{r}, \omega) = & \int_{S_s} (\tilde{P}_r^{fs}(\mathbf{r}, \mathbf{r}_s, \omega) \cdot \tilde{t}_r^n(\mathbf{r}_s, \omega) \\ & + \tilde{P}_z^{fs}(\mathbf{r}, \mathbf{r}_s, \omega) \cdot \tilde{t}_z^n(\mathbf{r}_s, \omega) \\ & + \tilde{L}_p^{fs}(\mathbf{r}, \mathbf{r}_s, \omega) \cdot \tilde{u}_z(\mathbf{r}_s, \omega) \\ & + \tilde{L}_p^{fs}(\mathbf{r}, \mathbf{r}_s, \omega) \cdot \tilde{u}_r(\mathbf{r}_s, \omega)) dS^s(\mathbf{r}_s), \end{aligned} \quad (40)$$

$$\begin{aligned} \tilde{v}_{\alpha, s}(\mathbf{r}, \omega) = & i\omega \int_{S_s} (\tilde{U}_{\alpha r}^{fs}(\mathbf{r}, \mathbf{r}_s, \omega) \cdot \tilde{t}_r^n(\mathbf{r}_s, \omega) \\ & + \tilde{P}_\alpha^{fs}(\mathbf{r}, \mathbf{r}_s, \omega) \cdot \tilde{u}_\alpha(\mathbf{r}_s, \omega) \\ & + \tilde{U}_{\alpha z}^{fs}(\mathbf{r}, \mathbf{r}_s, \omega) \cdot \tilde{t}_z^n(\mathbf{r}_s, \omega)) dS^s(\mathbf{r}_s), \\ & \alpha = z, r, \end{aligned} \quad (41)$$

$$\begin{aligned} \tilde{u}_{\alpha, s}(\mathbf{r}, \omega) = & \sum_{\beta=r, z} \int_{S_s} (\tilde{U}_{\alpha\beta}^{ss}(\mathbf{r}, \mathbf{r}_s, \omega) \cdot \tilde{t}_\beta^n(\mathbf{r}_s, \omega) \\ & - \tilde{T}_{\alpha\beta}^{n, ss}(\mathbf{r}, \mathbf{r}_s, \omega) \cdot \tilde{u}_\beta(\mathbf{r}_s, \omega)) dS^s(\mathbf{r}_s), \\ & \alpha = z, r, \end{aligned} \quad (42)$$

$$\tilde{L}_p^{fs}(\mathbf{r}, \mathbf{r}_s, \omega) = \rho_f c_f^2 \left( \frac{\partial \tilde{P}_r^{fs}}{\partial r} + \frac{\tilde{P}_r^{fs}}{r} + \frac{\partial \tilde{P}_z^{fs}}{\partial z} \right). \quad (43)$$

in which  $S_s$  indicates the cylindrical integration surface in the soil domain at  $r = r_s$ ,  $\tilde{L}_p$  is defined as the pressure operator using the strain-displacement relationships and Hooke's law, and  $\tilde{P}_\alpha^{fs}(\mathbf{r}, \mathbf{r}_s, \omega)$  is the pressure Green's function at the receiver  $r$  due to a unit load in  $\alpha$ -direction applied in the soil domain at  $\mathbf{r}_s$ ; note that  $\alpha$  here is also the direction of the displacement at the receiver point. The derivation of the soil source in  $\alpha$ -direction is given in Sec. IV A 2. As tangential stress vanishes in the fluid domain, the terms  $\tilde{T}_{rz}^{n, fs}(\mathbf{r}, \mathbf{r}_s, \omega)$  and  $\tilde{T}_{zr}^{n, fs}(\mathbf{r}, \mathbf{r}_s, \omega)$  vanish for the receiver in the fluid. Similarly, the stress tensors are obtained through the

constitutive relationships (Bakr, 1986) from the displacement functions and their derivatives.

### 3. Coupled acousto-elastodynamic BIE

By utilizing Betti's reciprocal theorem in elastodynamics (Beskos, 1987) and Green's theorem for acoustic problems (Jensen et al., 2011) as discussed in Secs. IV B 1 and IV B 2, the complete solution for the acousto-elastic domain reads

$$\begin{aligned} \tilde{u}_\alpha^\Xi(\mathbf{r}, \omega) = & \tilde{u}_\alpha^{\Xi, f}(\mathbf{r}, \omega) + \tilde{u}_\alpha^{\Xi, s}(\mathbf{r}, \omega) \\ = & \sum_{\beta=r, z} \int_{S^s} (\tilde{U}_{\alpha\beta}^{\Xi, s}(\mathbf{r}, \mathbf{r}_s, \omega) \cdot \tilde{t}_\beta^n(\mathbf{r}_s, \omega) \\ & - \tilde{T}_{\alpha\beta}^{n, \Xi, s}(\mathbf{r}, \mathbf{r}_s, \omega) \cdot \tilde{u}_\beta(\mathbf{r}_s, \omega)) dS^s(\mathbf{r}_s) \\ & + \int_{S^f} (\tilde{U}_{\alpha r}^{\Xi, f}(\mathbf{r}, \mathbf{r}_s, \omega) \cdot \tilde{p}(\mathbf{r}_s, \omega) \\ & - \tilde{T}_{\alpha r}^{n, \Xi, f}(\mathbf{r}, \mathbf{r}_s, \omega) \cdot \tilde{u}_r(\mathbf{r}_s, \omega)) dS^f(\mathbf{r}_s), \quad \mathbf{r} \in V, \end{aligned} \quad (44)$$

in which  $\mathbf{n}$  is the outward normal to the cylindrical boundary. The cylindrical surface in both the fluid and the soil domains needs to be discretized when employing the direct BEM associated with the acousto-elastic layered half-space Green's functions. The rule of thumb for using six elements per wavelength is adopted in the numerical integration of the line integral with the trapezoidal rule applied for the integration (Marburg, 2002). In the fluid domain, the integration is based on the shortest wavelength of the compressional waves. In the soil domain, the size of the element is governed by the shortest shear wavelength in accordance with the maximum frequency of interest.

## V. NUMERICAL CONSIDERATIONS

In this section, the numerical computation of the eigenvalues and the branch line integrations are presented, which determine the stability and convergence of the complete solution.

### A. Root-finding algorithm and poles

There are two challenges associated with the root-finding algorithm: (i) root-search in the complex wavenumber plane; (ii) presence of the branch cuts due to the soil half-space. Regarding the first item above, when dissipation is included in the form of complex Lamé constants, all eigenvalues become complex-valued.

This adds certain complexities in the root-searching in the complex  $k_r$  plane compared to the search of the eigenvalues for the lossless seabed case, which solely takes place on the real axis for poles related to propagating waves (Jensen et al., 2011; McCollom and Collis, 2014). Poles related to evanescent waves migrate from their original position in the complex wavenumber plane, which leads to the asymmetric distribution of the roots in the third and fourth quadrant of the complex wavenumber plane. In contrast, for lossless

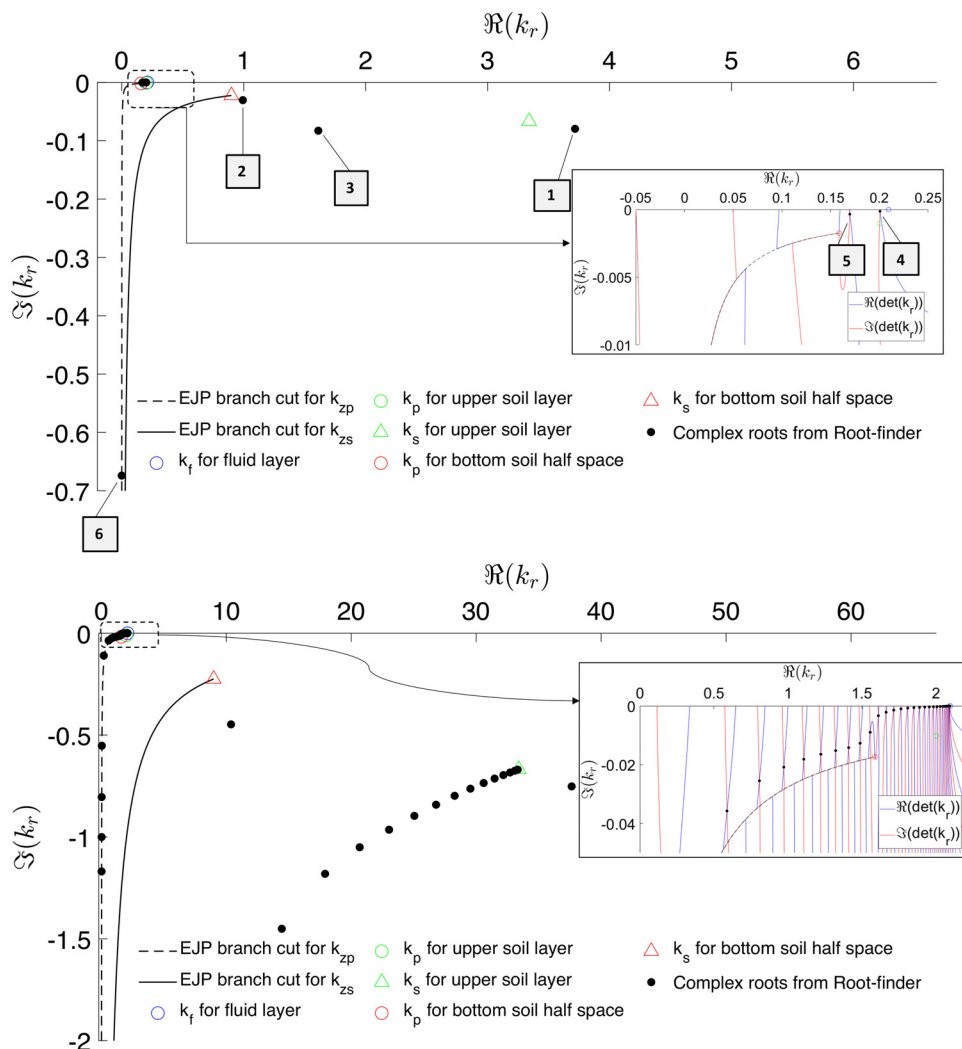


FIG. 5. (Color online) Complex roots for an acousto-elastic layered half-space with the parameters specified in Table IV in Sec. VII B at 50 Hz (top) and 500 Hz (bottom). The enlarged plots (within the box of the dashed line) verify the accuracy of the roots as the roots all locate at the intersections of the contour lines  $\Re(\det) = 0$  (blue line) and  $\Im(\det) = 0$  (red line).

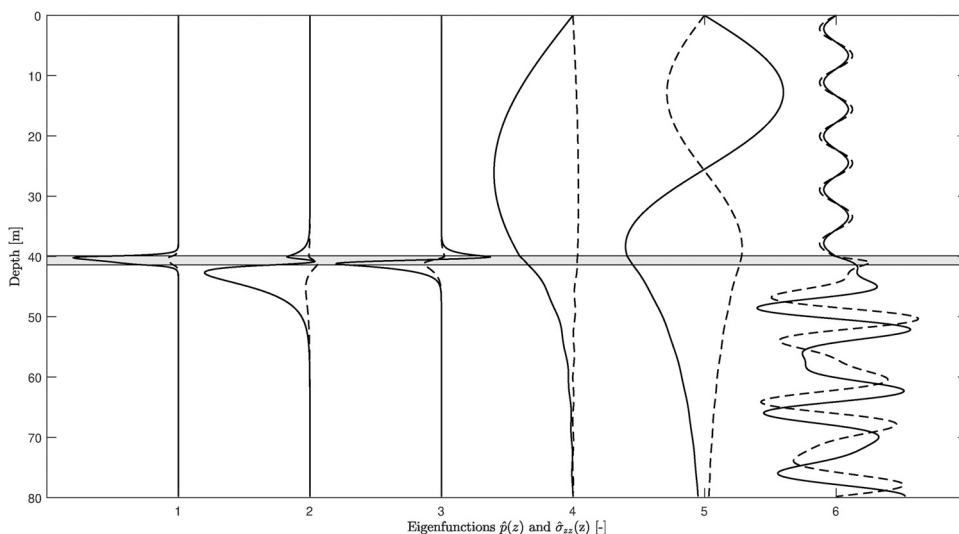


FIG. 6. Eigenfunctions of pressure and stress  $\sigma_{zz}$  for an acousto-elastic layered half-space at 50 Hz for the wavenumbers as indicated in Fig. 5(a): (1) the trapped mode associated with the Scholte wave; (2) the trapped mode associated with the Stoneley wave; (3) the trapped mode in the marine sediment layer; (4) and (5) two trapped modes in the fluid domain; (6) the leaky mode. The solid line indicates the real part of the eigenfunctions, and the dashed line represents the imaginary part.

TABLE I. Basic input parameters for the validation study of the Green's functions.

Parameter	Depth (m)	$\rho$ (kg/m <sup>3</sup> )	$c_L$ (m/s)	$c_T$ (m/s)	$\alpha_p$ (dB/ $\lambda$ )	$\alpha_s$ (dB/ $\lambda$ )
Fluid	40	1000	1500	—	—	—
Bottom soil	$\infty$	1908	1725	370	0.88	2.77

seabed, the symmetric feature requires the search of roots in only one of the quadrants.

Another challenge is associated with introducing the branch cuts when the bottom soil is modeled as a multilayered half-space. Compared to traditional root-searching for the acousto-elastic waveguide, this requires the root-finding to be performed on the correct Riemann surface across the branch cut to ensure the satisfaction of the radiation condition at  $z \rightarrow \infty$ . The configuration of the acousto-elastic half-space speeds up the root-searching, since only a finite number of poles are required for the convergence of the solution compared to the case of the waveguide.

In the computation presented in the sequel, the marine sediment layer is modeled by an almost fluidized thin soil layer at the upper part of the seabed, which is typically encountered in many offshore environments. This adds another challenge in the root-searching, which leads to a larger real part of the pole associated with Scholte waves at the fluid-soil interface, which are the slowest propagating waves present in the media.

In Fig. 5, the complex-valued roots are obtained for two excitation frequencies  $f = 50$  and 500 Hz. As shown in the enlarged plots, by solving the characteristic equation for the configuration summarized in Table IV, all poles are located at the intersections of the blue and red lines, indicating  $\Re(det) = \Im(det) = 0$ . The poles can be categorized into two types. One is related to the trapped modes, i.e., the first five modes shown in Fig. 6, in which vibrations of the system are localized within one of the acousto-elastic layers along with the depth or on one interface while decaying outside the finite area. The other one is related to the leaky modes, such as the sixth mode shown in Fig. 6, in which the energy radiates into the surrounding media (oscillatory patterns through the depth). As shown in Fig. 6, the trapped modes associated with Scholte and Stoneley waves are well captured. The gray-shaded area indicates

the 1.5 m-thick marine sediment layer, which plays a crucial role in channeling the energy between the water column and the seabed.

### B. The branch cuts and branch line integrals

Due to the presence of the soil half-space, the branch cuts are introduced and branch line integrations are required to obtain the exact solution for the Green's functions (Ewing *et al.*, 1957). The convergence of the solutions is influenced by choice of branch cuts. The criteria for assessing the convergence of the solution ensure that the ratio between the contribution of the branch line integration and the cumulative branch line integration is less than  $1E - 5$ . The most commonly applied ones are the Pekeris and EJP branch cuts (Bucker, 1979; Buckingham and Giddens, 2006; Ewing *et al.*, 1957; Stickler, 1975). The advantage of the EJP solution is that it solely requires the truncation of the branch line integrations. In contrast, the Pekeris solution needs to truncate both the vertical branch line integrations and normal modes (Bartberger, 1977). The latter one is valid only when the observation point is located at a sufficiently shallow depth or a sufficiently large range, which is due to the numerical instability of the solutions that may easily violate the radiation condition along the  $z$ -direction. In contrast, the representation of the EJP solution is convergent for all choices of range and depth coordinates, which ensures the smooth convergence of Green's tensors. In Fig. 5, most of the poles corresponding to the propagating waves that are trapped in the water column and the poles associated with leaky waves that radiate energy into the surrounding media are located on the principal Riemann surface. The pole associated with the Scholte wave is found on the third Riemann surface.

## VI. VALIDATION OF THE SOUND PROPAGATION MODULE

### A. Validation of the Green's functions

To validate the Green's tensors for a source located either in the fluid or in the soil, a case study is performed, and results are compared with the FE model build in the COMSOL Multiphysics<sup>®</sup> software (COMSOL AB, 2020).

The material properties in both models and the configuration of the acousto-elastic half-space for the sound

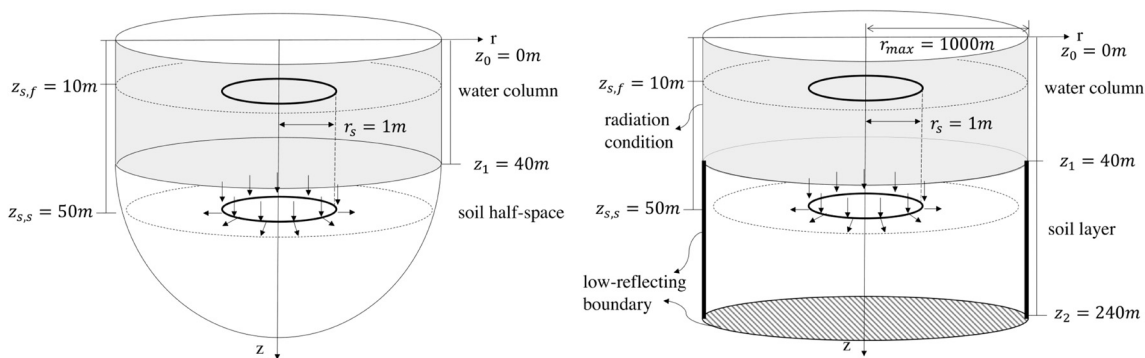


FIG. 7. Geometry of the model for ring load for the validation of the Green's tensors: semi-analytical model (sound propagation module) (left); finite-element model in COMSOL (right).

propagation model are given in Table I in accordance with Fig. 7. In the sound propagation module, the domain is modeled as an acoustic layer overlying an elastic half-space with pressure release boundary at the sea surface and the interface conditions at the seabed as presented in Sec. IV A. The radiation conditions are satisfied exactly at both  $r \rightarrow \infty$  and  $z \rightarrow \infty$ . In the COMSOL model, the acousto-elastic waveguide is truncated at 200 m below the seabed by a low-reflecting boundary as indicated in Fig. 7, which is used to reduce the computational domain to a practical size while ensuring the satisfaction of the radiation condition within an accurate range. In practice, the low-reflecting boundary works ideally for waves propagating in the normal direction to the boundary as it creates a perfect impedance match for compressional and shear waves. The dissipation in the soil is expressed by the frequency-dependent complex compressional and shear wave speeds in both models. In Fig. 7,  $z_{s,f}$  and  $z_{s,s}$  define the depth of the loading level,  $r_s$  is the radius of the ring source,  $z_1$  is the depth of the water column, and  $z_2$  in the COMSOL model gives the depth of the bottom low-reflecting boundary.

The predictions of the two models are compared for three load cases at three excitation frequencies of 30 Hz, 125 Hz, and 1 kHz, namely a circular source in the fluid and a ring load in  $r$ - and  $z$ -directions in the soil, named after **R**-ring and **Z**-ring load in Fig. 8. The response on the cylindrical surface at  $r = 2$  m is shown in Fig. 8. The numerical results from both models are in good agreement for various loading cases, which validates the sound propagation module.

**B. Validation of boundary integrals**

In this section, to validate the boundary integral formulations, a theoretical case study is performed. Based on the results in Sec. VI A, the Green’s functions have been verified. As shown in Fig. 9, four scenarios are examined: (i) the direct method, to generate the wavefield at  $r = 200$  m from the Green’s function for a source positioned either in the fluid or in the soil; (ii)–(iv) the BIE method, to generate the wavefield at  $r = 200$  m through BIE with the input on the cylindrical boundary at (ii)  $r_s = 5$  m, (iii)  $r_s = 20$  m, and (iv)  $r_s = 40$  m, which was obtained from the Green’s function for a point source positioned either in the fluid or in the soil. The material parameters and geometry of the acousto-elastic media are given in Table II.

As discussed in Sec. IV B, the sound propagation module is based on a BIE, in which the input is obtained from the source generation module. In this case, the sound generation module delivers the Green’s function for a point source. The input is obtained on a cylindrical surface, as indicated by the dark gray surface shown in Fig. 9. The results are presented for three excitation frequencies 30 Hz, 125 Hz, and 1 kHz for both scenarios as shown in Fig. 10. In the presence of either fluid or soil source in the domain, the solutions show a good agreement between two approaches, which validates the BIE formulation for the sound

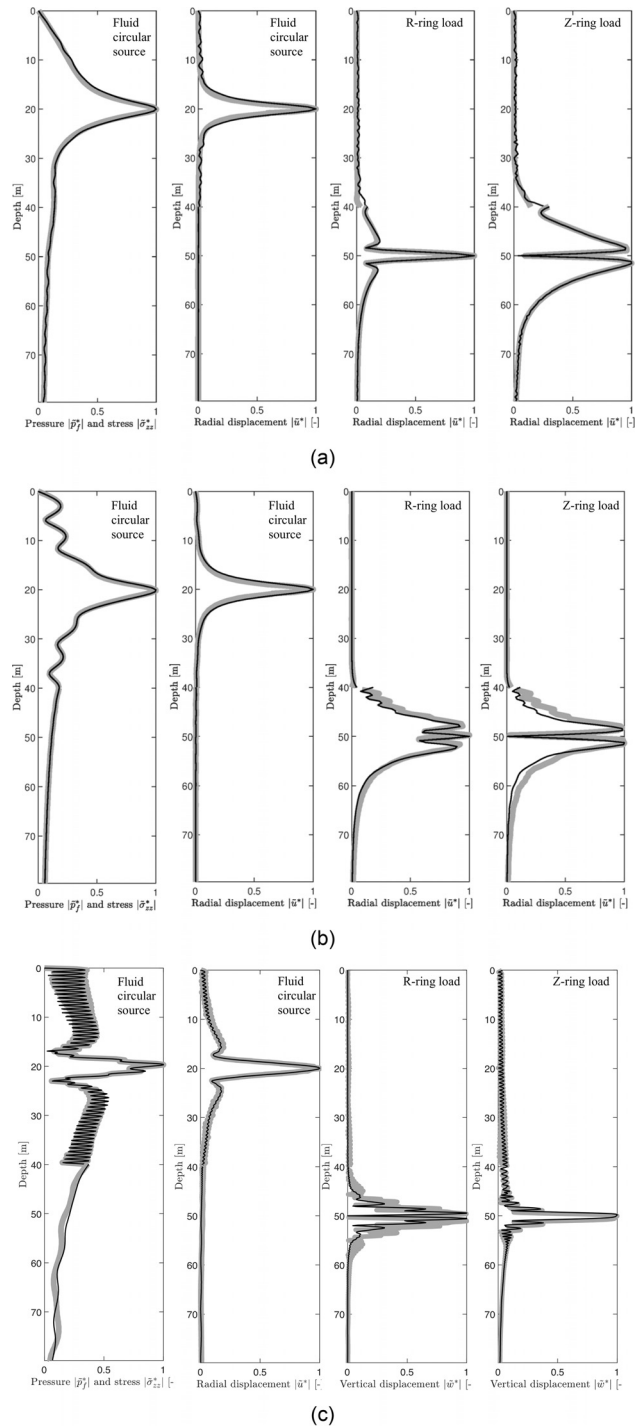


FIG. 8. Comparison of Green’s tensors from a sound propagation model and FE model for a point source at three excitation frequencies 30 Hz, 125 Hz, and 1 kHz as indicated in Fig. 7: the pressure and normal stress for a fluid circular source; the radial displacement for a fluid circular source; the radial displacement for a **R**-ring load in the soil; the radial displacement for a **Z**-ring load in the soil at (a)  $f = 30$  Hz, (b)  $f = 125$  Hz, and (c)  $f = 1000$  Hz. The thin black line indicates the results from the sound propagation model, and the thick gray line represents the numerical results from the COMSOL model.

propagation model. Figure 10 also shows that the BIE solutions agree well at different coupling radius  $r_s$ , which indicates that the influence of the choice of  $r_s$  is insignificant and the solutions are stable.

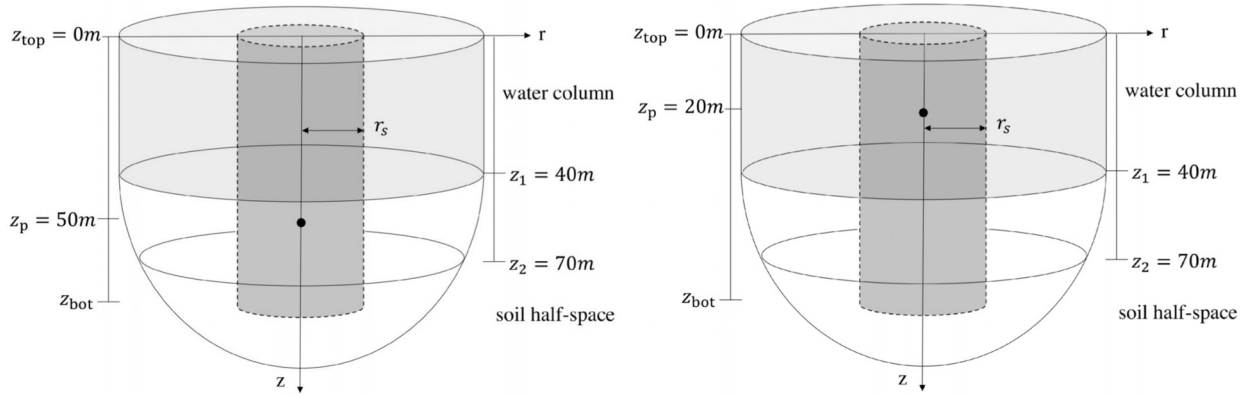


FIG. 9. Geometry of the model for the validation of the boundary integral formulations for a point source positioned as follows: in the seabed as an R-load soil source (left); in the fluid domain as a pressure source (right).

**VII. NUMERICAL RESULTS**

In this section, the solution of the complete model is examined for several benchmark cases: (a) a theoretical bench scenario from the COMPILE workshop with numerical data from several different numerical models (Lippert *et al.*, 2016); (b) a validation case with measurement data from a recent offshore wind farm in the German North Sea. The material and geometrical parameters are obtained from the literature (Lippert *et al.*, 2016) for case (a) and available geotechnical reports at the pile-installation site for case (b). The results were obtained on a quad-core 3.6GHz processor running the 64-bit Windows operating system. The total computation time for the solution is the sum of  $T_{total} = t_f^{CPU} \cdot N_f = t_{f,g}^{CPU} \cdot N_f \cdot N_g$ , in which  $N_f$  is the number of frequencies considered,  $N_g$  is the number of grid points considered in which output is required,  $t_f^{CPU}$  represents the average computation time per frequency, and  $t_{f,g}^{CPU}$  represents the average computation time per output grid per frequency.

**A. Theoretical benchmark case COMPILE I**

In this section, the case examined is based on a generic theoretical benchmark case for underwater noise prediction for offshore pile driving. At the COMPILE workshop in 2014, seven different modeling approaches were presented (Lippert *et al.*, 2016). As given in Table III, the model consists of a pile with a Young’s modulus of 210 GPa, a Poisson ratio of 0.3, and a fluid layer overlying a soil half-space. The forcing function is reported in Lippert *et al.* (2016), and the computation involves 3000 equally spaced frequencies ranging from ~0.8333 to 2500 Hz. The average computation time for the solution per output grid per frequency is  $t_{f,g}^{CPU} = 0.02$  s. In the models at the COMPILE workshop, the material damping in the pile is introduced in

the embedded section of the pile through compressional and shear wave speed, which is different from the approach of introducing a frequency independent structural loss factor for the shell structure used in this model.

The zero-to-peak pressure level ( $L_{p,pk}$ ) in dB re 1  $\mu$ Pa and the SEL in units of dB re 1  $\mu$ Pa<sup>2</sup>s are defined as (Lippert *et al.*, 2016)

$$L_{p,pk} = 20 \log \left( \frac{\max|p(t)|}{p_0} \right), \quad SEL = 10 \log \left( \int_{T_1}^{T_2} \frac{p^2(t)}{p_0^2} dt \right), \quad (45)$$

in which  $T_1$  and  $T_2$  are the starting and ending of the predicted time signature with the sound event in between and pulse duration  $T_0 = T_2 - T_1$  being 1 s, and  $p_0 = 10^{-6}$  Pa is the reference underwater sound pressure.

The evolution of the pressure in time is shown in Fig. 11 for a point positioned 1 m above the seabed at 750 and 1500 m radial distances from the pile. The  $L_{p,pk}$  and SEL of receiver points at radial distances up to 750 m are shown in Fig. 11. As can be seen, the predicted SEL and  $L_{p,pk}$  at 750 m from the pile are 164.9 and 189.6 dB, respectively, while the arithmetic mean values from COMPILE are 166.7 dB for the SEL and 191.2 dB for the  $L_{p,pk}$ . At 1500 m, the predicted SEL and  $L_{p,pk}$  are 160.2 and 181 dB, respectively, while the arithmetic mean values from COMPILE are 161.3 dB for the SEL and 184 dB for the  $L_{p,pk}$ . Thus, the accuracy of the computation is less than  $\pm 2$  dB for SEL and around  $\pm 3$  dB for  $L_{p,pk}$  when compared to the arithmetic mean values determined by the various models at the COMPILE workshop. As expected, the variation of SEL along the radial direction is smoother, while the prediction of the  $L_{p,pk}$  is more oscillatory mainly because the latter reflects a single peak of the pressure, which can be influenced by many factors and is more sensitive to the location of the observation point.

The comparison of the evolution of the pressure in time at a receiver position of  $r = 11$  m and  $z = 5$  m in the vicinity of the pile is shown in Fig. 12 for the comparison of different modeling techniques. The results show that all models can predict the arrivals of the primary Mach cones. The

TABLE II. Basic input parameters for the validation study.

Parameter	Depth (m)	$\rho$ (kg/m <sup>3</sup> )	$c_L$ (m/s)	$c_T$ (m/s)	$\alpha_p$ (dB/ $\lambda$ )	$\alpha_s$ (dB/ $\lambda$ )
Fluid	40	1000	1500	—	—	—
Upper soil	30	1888	1775	198	0.2	0.8
Bottom soil	$\infty$	1950	1976	370	1.0	2.5

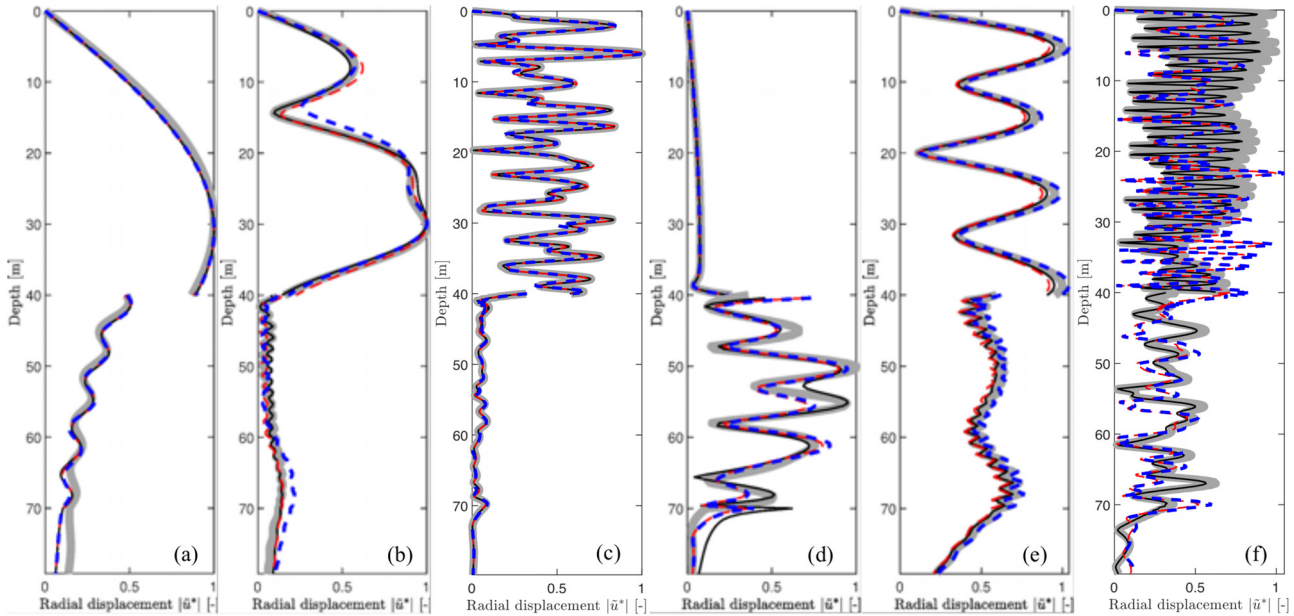


FIG. 10. (Color online) Comparison for the results based on direct method (Green’s function) and boundary element method for a ring load at three excitation frequencies 30 Hz, 125 Hz, and 1 kHz as indicated in Fig. 9: the radial displacement for a fluid circular source at (a)  $f = 30$  Hz, (b)  $f = 125$  Hz, and (c)  $f = 1000$  Hz; the radial displacement for an **R**-ring load in the soil at (d)  $f = 30$  Hz, (e)  $f = 125$  Hz, and (f)  $f = 1000$  Hz. The thin black line indicates results from BIE at  $r_s = 5$  m, the red dashed line indicates results from BIE at  $r_s = 20$  m, the blue dashed line indicates results from BIE at  $r_s = 40$  m, and the thick gray line represents the results from the Green’s function (direct method).

difference between this model and the models at the COMPILE workshop is mainly due to the different modeling approaches of the seabed; the latter modeled the seabed as equivalent fluid, while this model describes the soil as an elastic medium. The modeled pressure field in the time domain is found to be in relatively good agreement with the numerical results from the JASCO model compared to the other numerical models because the JASCO model uses a time-domain finite-difference model for pile vibrations with the pile modeled as a cylindrical thin shell in a similar approach as in this model.

Figure 13 shows the pressure levels (dB re  $1 \mu\text{Pa}^2/\text{Hz}$ ) in one-third octave bands at various radial distances from the pile. Assuming that the energy in all the defined bandwidths (one-third octave) results from an effective source, the bandwidth energies add directly to give the total energy in one frequency band. The derivation of the sound pressure level (SPL) in the unit of dB re  $1 \mu\text{Pa}^2\text{s}^{-1}$  reads

$$\text{SPL}_{1/3\text{octave}} = 10 \log_{10} \sum_{i=m}^n \left( \frac{|\tilde{p}_i(\omega)|^2}{P_0^2} \right). \quad (46)$$

TABLE III. Basic input parameters for the COMPILE benchmark case (Lippert et al., 2016).

Parameter	Pile	Parameter	Fluid	Soil
Length (m)	25	Depth (m)	10	$\infty$
Density ( $\text{kg/m}^3$ )	7850	Density ( $\text{kg/m}^3$ )	1025	2000
Outer diameter (m)	2	$c_p$ (m/s)	1500	1800
Wall thickness (mm)	50	$c_s$ (m/s)	—	170
Final penetration depth (m)	15	$\alpha_p$ (dB/ $\lambda$ )	—	0.469
Structural damping (—)	0.001	$\alpha_s$ (dB/ $\lambda$ )	—	1.69

As can be seen in Fig. 13, the spectrum shows that most of the energy is concentrated at the critical frequency range (being  $0.5f_r \sim 0.8f_r$ ) associated with the ring frequency of the pile ( $f_r = 857$  Hz), which is consistent with the

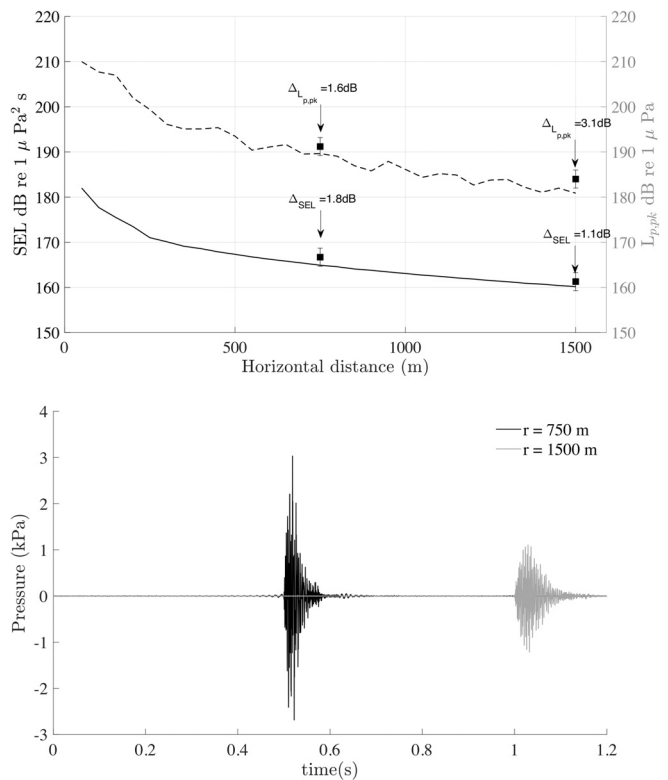


FIG. 11. COMPILE: Comparison of SEL and  $L_{p,pk}$  at several radial distances from the pile and 1 m above the seabed (top); computed time histories of the pressure in the water at various radial distances at 1 m above the seabed (bottom).

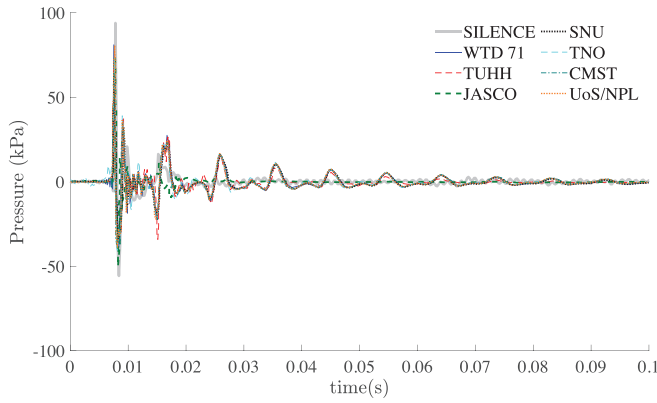


FIG. 12. (Color online) COMPPILE scenario: Comparison of the evolution of the pressure field at a receiver position of  $r = 11$  m and  $z = 5$  m.

characteristics of the pile dimension and the noise spectrum discussed in Tsouvalas (2020).

### B. Offshore wind farm in German North Sea

In this section, noise predictions using the developed model are compared with measured noise data collected during installation of a foundation pile in the German North Sea in 2018. The measurement of the hydro-sound emissions was conducted at horizontal distances of 750 and 1500 m from the pile and at a water depth of about 2 m above the seabed. The material properties and the geometry of the model are given in Table IV. The material of the pile is chosen to be standard steel with a Young's modulus of 210 GPa and a Poisson ratio of 0.3. The seabed consists of a thin marine sediment layer overlying a stiffer soil half-space. The upper thin layer corresponds to a water-saturated marine sediment, whereas the bottom layer corresponds to a very fine sand layer. The actual penetration depth of the pile was around 32.7 m. The forcing function (in MN) is defined as the smoothed exponential impulse,

$$F(t) = \begin{cases} F_A \sin(F_B(t - t_0))e^{-FC(t-t_0)}, & t_0 < t < t_1, \\ 0, & t < t_0 \text{ or } t > t_1, \end{cases} \quad (47)$$

in which  $t_0$  being 0.001 s represents the start time and  $t_1$  being 0.05 s represents the end time of the pulse. The other parameters in the forcing function are given as follows:  $F_A = 503$ ,  $F_B = 149$ ,  $FC = 150$ . This force correspondent generates approximately 1750 KJ blow energy into the system,

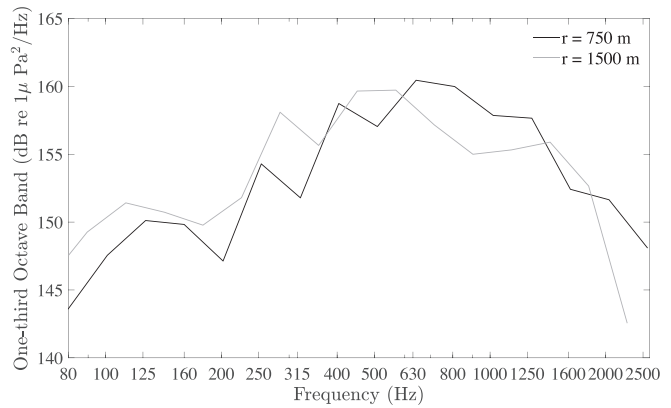


FIG. 13. COMPPILE scenario: One-third octave band spectrum for a point positioned 1 m above the seabed in the fluid and at  $r = 750$  and 1500 m from the pile.

which is in line with the measured value. The computation involves 2000 frequencies at 0.625-Hz steps ranging from  $\sim 0.625$  to 1250 Hz. The computation time for the solution per frequency per output grid in average is  $t_{f,g}^{CPU} = 0.022$  s.

In Fig. 14 (bottom), the evolution of the pressure in time is shown for a point positioned 2 m above the seabed at 750 and 1500 m radial distances from the pile. As can be seen, the arrival of the pressure cones is at around 0.5 and 1 s, respectively, after the impact of the pile, which is in line with the expectations regarding the arrival time of the direct sound waves traveling with the speed of sound in the water at those distances. The  $L_{p,pk}$  and the SEL of receiver points at radial distances up to 1500 m are shown in Fig. 14 (top). As can be seen, the differences between the predicted SEL and the averaged measured values are 1 and 0.5 dB at 750 and 1500 m radial distances from the pile, respectively. The SEL indicates the averaged amount of energy radiated into the surrounding media, and  $L_{p,pk}$  evaluates the impulsiveness of the pressure waves from the pile. In practice, the hydrophones were not deployed exactly at 750 and 1500 m from the pile but with a deviation of up to 2 m; therefore, both the upper and lower bound of the SEL and  $L_{p,pk}$  from at 750 and 1500 m horizontal distance from the pile and 2 m above the seabed are used as the comparison with a measurement error of  $\pm 2$  dB. The results verify the validity of the complete model, which can provide predictions that lie within the accuracy of the measurement equipment ( $\pm 1$  or 2 dB). As can be seen in Fig. 15, the spectrum shows that most of the energy is concentrated at low frequencies and up to around 400 Hz.

TABLE IV. Basic input parameters for the simulations at the offshore wind farm in the German North Sea.

Parameter	Pile	Parameter	Fluid	Upper soil	Bottom sediment
Length (m)	76.9	Depth (m)	39.9	1.5	$\infty$
Density ( $\text{kg/m}^3$ )	7850	$\rho$ ( $\text{kg/m}^3$ )	1000	1670	1950
Outer diameter (m)	8	$c_p$ (m/s)	1500	1560	1979
Wall thickness (mm)	90	$c_s$ (m/s)	—	94	349
Final penetration depth (m)	32.7	$\alpha_p$ (dB/ $\lambda$ )	—	0.55	0.27
Maximum blow energy (kJ)	1750	$\alpha_s$ (dB/ $\lambda$ )	—	1.36	1.09

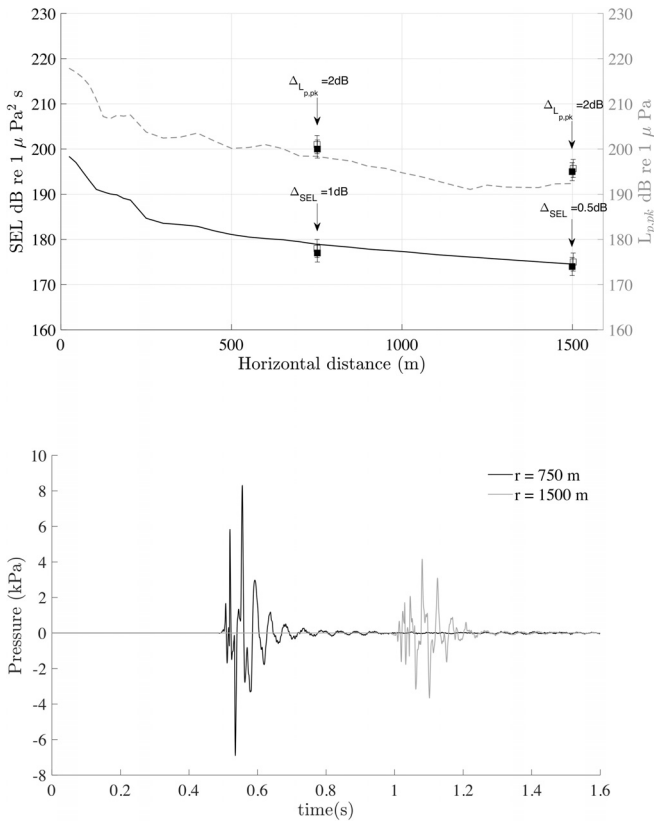


FIG. 14. Offshore wind farm scenario: Pressure field at a point located at 2 m above the seabed at various radial distances from the pile: comparison of SEL and  $L_{p,pk}$ , in which the black error bar indicates the lower bound of sound levels from measurement and the hollow error bar represents the upper bound (top); computed time histories of the pressure in the water (bottom).

At around 10- and 20-m pile penetration depth, the blow energy recorded was 550 and 1350 kJ, respectively. Based on the measurement data, SEL and  $L_{p,pk}$  are obtained for these two cases at 750 and 1500 m from the pile. As can be seen in Fig. 16, the predicted SEL and  $L_{p,pk}$  are consistent with the recorded sound levels. For the pile with 10-m penetration depth, the deviation to the central measured data point is both 2 dB for SEL and  $L_{p,pk}$  at 750 m and is 1 dB for SEL and 3 dB for  $L_{p,pk}$  at 1500 m. For the pile with 20-m penetration depth, the deviation to the central measured data

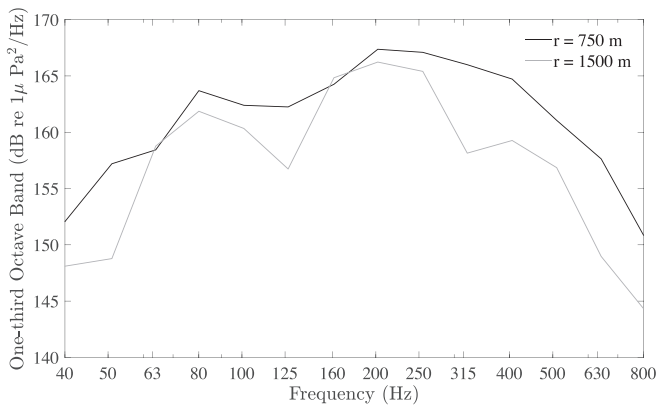


FIG. 15. Offshore wind farm scenario: One-third octave band spectrum for a point positioned 2 m above the seabed in the fluid and at  $r = 1500$  m from the pile.

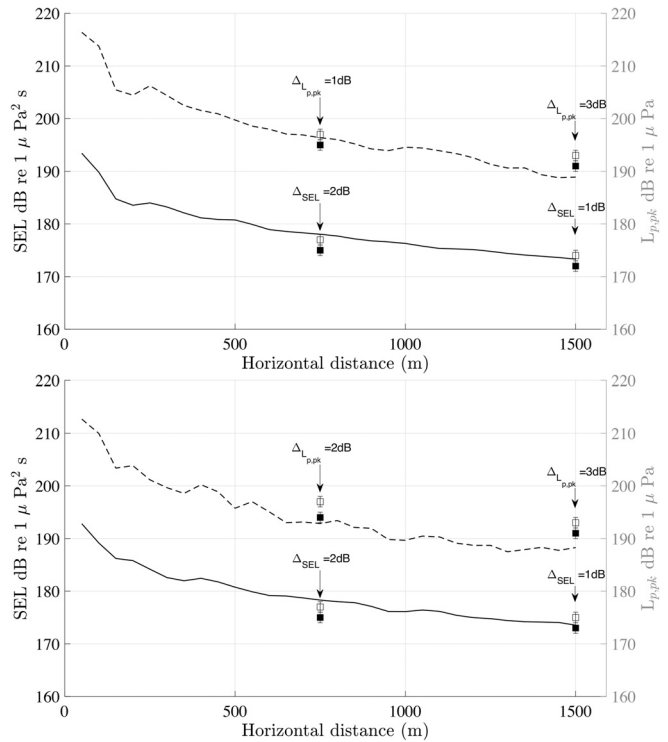


FIG. 16. Offshore wind farm scenario: Comparison of SEL and  $L_{p,pk}$  for the pressure field at a point located at 2 m above the seabed at various radial distances from the pile: 20-m pile penetration depth (top); 10-m pile penetration depth, in which the black error bar indicates the lower bound of sound levels from measurement and the hollow error bar represents the upper bound (bottom).

point is 2 dB for SEL and 1 dB for  $L_{p,pk}$  at 750 m and 1 dB for SEL and 3 dB for  $L_{p,pk}$  at 1500 m.

As discussed earlier in Fig. 2, the variation of the penetration depth of the pile does not influence the eigenvalues of the shell and acousto-elastic media. Therefore, the eigenvalue problems do not need to be recomputed for each frequency. Instead, the modal analysis and the final response of the coupled system solely need to be solved, which largely reduces the computation time as presented in Fig. 17. This reduction in the computation time as depicted by the two bars in Fig. 17 shows the advantage of the model when used in parametric studies.

### VIII. CONCLUSIONS

The paper establishes a computationally efficient method for noise predictions over large horizontal distances in offshore pile driving. The complete model comprises a sound generation module and a sound propagation module. The former aims at describing accurately the pile-soil-water interaction and the wavefield generated at the surrounding acousto-elastic domain in the vicinity of the pile. The latter aims to propagate this wavefield at larger distances from the pile (up to a few kilometers), provided that bathymetry changes are insignificant. The mathematical statement of the complete problem is presented, and the adopted method of solution is described in great detail. The direct BIE formulation is used to couple the two modules and propagate the wavefield from the vicinity of the pile to larger distances. Numerical accuracy

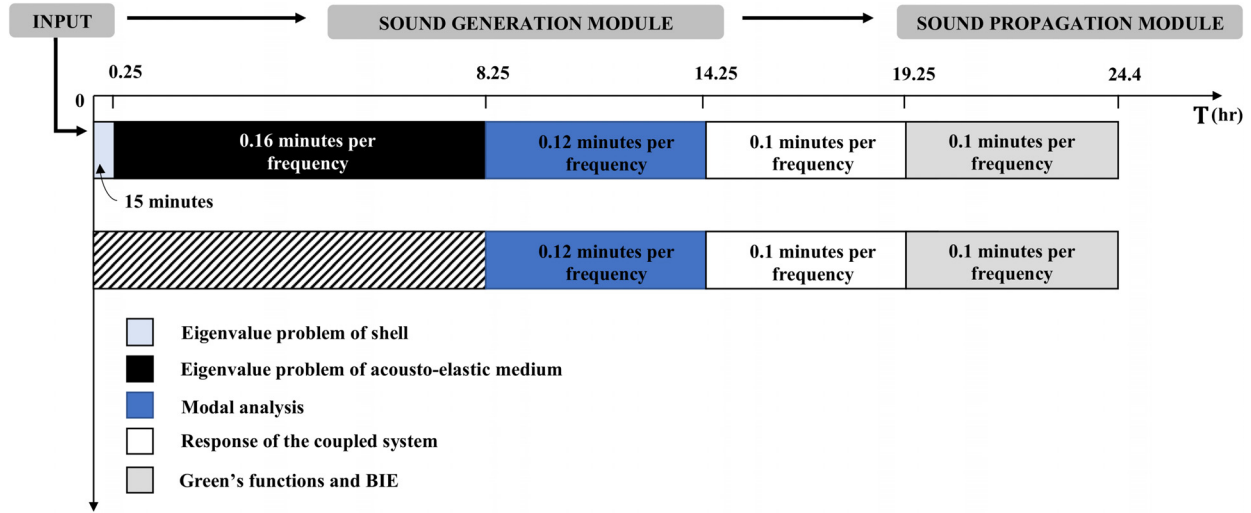


FIG. 17. (Color online) Offshore wind farm scenario: Activity plot for the computational time of individual blocks in the model including central processing unit (CPU) time per frequency and total execution time T, in which the first bar indicates the complete simulation and the second bar represents the computation time for 10- or 20-m pile penetration depth.

and solution stability are discussed in great detail together with the different physical interpretations of the various eigenmodes. One theoretical case study is examined to benchmark the model by comparison with seven different modeling techniques. Noise predictions are then performed for a pile-installation campaign in 2018, and the results are compared to the measurement data for the pile driven at various penetration depths. The results show that the model is able to capture the SEL within an accuracy of 2 dB and the  $L_{p,pk}$  within an accuracy of around 3 dB for distances up to 1500 m from the pile at various penetration depths. The computational time is presented for each case study, which indicates the efficiency of the model. To examine the influence of different input parameters for the noise prediction, e.g., different penetration depth, various forcing functions, various sizes of the pile, etc., it requires solely parts of the model to be recomputed, which largely reduces the computational effort and later can be used in probabilistic analysis of noise prediction.

### ACKNOWLEDGMENTS

This research was supported by China Scholarship Council (CSC), which financed the research project (Grant No. 201707720006) on the development of a generic underwater noise prediction model for offshore activities. The authors also wish to express their thanks to Van Oord and specifically to Remco Huizer, Wouter Dirks, and Roeland Ris for supporting this research and for providing data from a recent offshore installation campaign. For questions related to the data please contact the Noise Desk of Van Oord (NoiseDesk@vanoord.com).

### APPENDIX

By substituting the expressions into the boundary and interface conditions shown in Eqs. (9)–(12), the final set of linear algebraic equations with unknowns  $A_i^g$  for  $i = 1, 2, \dots, 4N + 2$  reads

$$\frac{1}{-\rho\omega^2} \frac{e^{-ik_{z,f}(z_s-z_0)}}{4\pi ik_{z,f}} + A_1^g e^{ik_{z,f}z} + A_2^g e^{-ik_{z,f}z_0} = 0, \quad (A1)$$

$$\begin{aligned} & \frac{e^{-ik_{z,f}(z_1-z_s)}}{4\rho\omega^2\pi} - A_1^g ik_{z,f} e^{-ik_{z,f}z_1} + A_2^g ik_{z,f} e^{k_{z,f}D_1 i} \\ &= -A_3^g ik_{z,p_1} e^{-ik_{z,p_1}z_1} + A_4^g ik_{z,p_1} \cdot e^{k_{z,p_1}z_1 i} \\ & \quad - A_5^g k_{z,s_1}^2 e^{-ik_{z,s_1}z_1} - A_6^g k_{z,s_1}^2 e^{k_{z,s_1}z_1 i} \\ & \quad + k_{s_1}^2 (A_5^g e^{-ik_{z,s_1}z_1} + A_6^g e^{k_{z,s_1}z_1 i}), \end{aligned} \quad (A2)$$

$$\begin{aligned} & \frac{e^{-ik_{z,f}(z_1-z_s)} i}{4\rho\omega^2\pi k_{z,f}} + A_1^g e^{-ik_{z,f}z_1} + A_2^g e^{k_{z,f}z_1 i} \\ &= -\frac{1}{\rho\omega^2} \left( -\lambda_1 k_{p_1}^2 [A_3^g e^{-ik_{z,p_1}z_1} + A_4^g e^{k_{z,p_1}z_1 i}] \right. \\ & \quad + 2\mu_1 [-A_3^g k_{z,p_1}^2 e^{-ik_{z,p_1}z_1} - A_4^g k_{z,p_1}^2 e^{k_{z,p_1}z_1 i} \\ & \quad + A_5^g k_{z,s_1}^3 e^{-ik_{z,s_1}z_1} i - A_6^g k_{z,s_1}^3 e^{k_{z,s_1}z_1 i} i \\ & \quad \left. + k_{s_1}^2 (-A_5^g k_{z,s_1} e^{-ik_{z,s_1}z_1} i + A_6^g k_{z,s_1} e^{k_{z,s_1}z_1 i} i) \right), \end{aligned} \quad (A3)$$

$$\begin{aligned} & -2iA_3^g k_{z,p_1} e^{-ik_{z,p_1}z_1} + 2iA_4^g k_{z,p_1} e^{ik_{z,p_1}z_1} \\ & - 2A_5^g k_{z,s_1}^2 e^{-ik_{z,s_1}z_1} - 2A_6^g k_{z,s_1}^2 e^{ik_{z,s_1}z_1} \\ & + k_{s_1}^2 (A_5^g e^{-ik_{z,s_1}z_1} + A_6^g e^{ik_{z,s_1}z_1}) = 0, \end{aligned} \quad (A4)$$

$$\begin{aligned} & -A_{4j+3}^g ik_{z,p_{j+1}} e^{-ik_{z,p_{j+1}}z_{j+1}} + A_{4j+4}^g ik_{z,p_{j+1}} e^{ik_{z,p_{j+1}}z_{j+1}} \\ & - A_{4j+5}^g k_{z,s_{j+1}}^2 e^{-ik_{z,s_{j+1}}z_{j+1}} - A_{4j+5}^g k_{z,s_{j+1}}^2 e^{ik_{z,s_{j+1}}z_{j+1}} \\ & + k_{s_{j+1}}^2 (A_{4j+5}^g e^{-ik_{z,s_{j+1}}z_{j+1}} + A_{4j+6}^g e^{ik_{z,s_{j+1}}z_{j+1}}) \\ &= -A_{4j-1}^g ik_{z,p_j} e^{-ik_{z,p_j}z_{j+1}} + A_{4j}^g ik_{z,p_j} e^{ik_{z,p_j}z_{j+1}} \\ & - A_{4j+1}^g k_{z,s_j}^2 e^{-ik_{z,s_j}z_{j+1}} - A_{4j+1}^g k_{z,s_j}^2 e^{ik_{z,s_j}z_{j+1}} \\ & + k_{s_j}^2 (A_{4j+1}^g e^{-ik_{z,s_j}z_{j+1}} + A_{4j+2}^g e^{ik_{z,s_j}z_{j+1}}), \quad j = 1, \dots, N, \end{aligned} \quad (A5)$$

$$\begin{aligned}
 & A_{4j+3}^g e^{-ik_{z,p_{j+1}} z_{j+1}} + A_{4j+4}^g e^{ik_{z,p_{j+1}} z_{j+1}} \\
 & - A_{4j+5}^g ik_{z,s_{j+1}} e^{-ik_{z,s_{j+1}} z_{j+1}} + A_{4j+6}^g ik_{z,s_{j+1}} e^{ik_{z,s_{j+1}} z_{j+1}} \\
 & = A_{4j-1}^g e^{-ik_{z,p_j} z_j} + A_{4j}^g e^{ik_{z,p_j} z_j} - A_{4j+1}^g ik_{z,s_j} e^{-ik_{z,s_j} z_j} \\
 & + A_{4j+2}^g ik_{z,s_j} e^{ik_{z,s_j} z_j}, \quad j = 1, \dots, N, \tag{A6}
 \end{aligned}$$

$$\begin{aligned}
 & -\lambda_{j+1} k_{p_{j+1}}^2 (A_{4j+3} e^{-ik_{z,p_{j+1}} z_{j+1}} + A_{4j+4} e^{ik_{z,p_{j+1}} z_{j+1}}) \\
 & + 2\mu_{j+1} (-A_{4j+3} k_{z,p_{j+1}}^2 \cdot e^{-ik_{z,p_{j+1}} z_{j+1}} \\
 & - A_{4j+4} k_{z,p_{j+1}}^2 e^{ik_{z,p_{j+1}} z_{j+1}} + A_{4j+5} ik_{z,s_{j+1}}^3 e^{-ik_{z,s_{j+1}} z_{j+1}} \\
 & - A_{4j+6} ik_{z,s_{j+1}}^3 \cdot e^{ik_{z,s_{j+1}} z_{j+1}} + k_{s_{j+1}}^2 (-A_{4j+5} ik_{z,s_{j+1}} \\
 & \times e^{-ik_{z,s_j} z_{j+1}} + A_{4j+6} ik_{z,s_{j+1}} e^{ik_{z,s_{j+1}} z_{j+1}})) \\
 & = -\lambda_j k_{p_j}^2 (A_{4j-1} e^{-ik_{z,p_j} z_{j+1}} + A_{4j} e^{ik_{z,p_j} z_{j+1}}) \\
 & + 2\mu_j (-A_{4j-1} k_{z,p_j}^2 e^{-ik_{z,p_j} z_{j+1}} - A_{4j} k_{z,p_j}^2 e^{ik_{z,p_j} z_{j+1}} \\
 & + A_{4j+1} ik_{z,s_j}^3 e^{-ik_{z,s_j} z_{j+1}} - A_{4j+2} ik_{z,s_j}^3 e^{ik_{z,s_j} z_{j+1}} \\
 & + k_{s_j}^2 (-A_{4j+1} ik_{z,s_j} e^{-ik_{z,s_j} z_{j+1}} + A_{4j+2} ik_{z,s_j} e^{ik_{z,s_j} z_{j+1}})), \\
 & j = 1, \dots, N, \tag{A7}
 \end{aligned}$$

$$\begin{aligned}
 & \mu_{j+1} (-2iA_{4j+3}^g k_{z,p_{j+1}} e^{-ik_{z,p_{j+1}} z_{j+1}} + 2iA_{4j+4}^g k_{z,p_{j+1}} e^{ik_{z,p_{j+1}} z_{j+1}} \\
 & - 2A_{4j+5}^g k_{z,s_{j+1}}^2 e^{-ik_{z,s_{j+1}} z_{j+1}} - 2A_{4j+6}^g k_{z,s_{j+1}}^2 e^{ik_{z,s_{j+1}} z_{j+1}} \\
 & + k_{s_{j+1}}^2 (A_{4j+5}^g e^{-ik_{z,s_{j+1}} z_{j+1}} + A_{4j+6}^g e^{ik_{z,s_{j+1}} z_{j+1}})) \\
 & = \mu_j (-2iA_{4j-1}^g k_{z,p_j} e^{-ik_{z,p_j} z_{j+1}} + 2iA_{4j}^g k_{z,p_j} e^{ik_{z,p_j} z_{j+1}} \\
 & - 2A_{4j+1}^g k_{z,s_j}^2 e^{-ik_{z,s_j} z_{j+1}} - 2A_{4j+2}^g k_{z,s_j}^2 e^{ik_{z,s_j} z_{j+1}} \\
 & + k_{s_j}^2 (A_{4j+1}^g e^{-ik_{z,s_j} z_{j+1}} + A_{4j+2}^g e^{ik_{z,s_j} z_{j+1}})), \quad j = 1, \dots, N. \tag{A8}
 \end{aligned}$$

Abramowitz, M., and Stegun, I. A. (1964). *Handbook of Mathematical Functions with Formulas, Graphs, and Mathematical Tables* (National Bureau of Standards, Washington, DC).

Achenbach, J. D. (1973). *Wave Propagation in Elastic Solids* (North-Holland, Amsterdam).

Ainslie, M. A., Halvorsen, M. B., Müller, R. A. J., and Lippert, T. (2020). "Application of damped cylindrical spreading to assess range to injury threshold for fishes from impact pile driving." *J. Acoust. Soc. Am.* **148**(1), 108–121.

Bailey, H., Senior, B., Simmons, D., Rusin, J., Picken, G., and Thompson, P. M. (2010). "Assessing underwater noise levels during pile-driving at an offshore windfarm and its potential effects on marine mammals." *Mar. Pollut. Bull.* **60**(6), 888–897.

Bakr, A. A. (1986). *Axisymmetric Potential Problems* (Springer, Berlin), pp. 6–38.

Bartberger, C. L. (1977). "Comparison of two normal-mode solutions based on different branch cuts." *J. Acoust. Soc. Am.* **61**(6), 1643–1643.

Beskos, D. E. (1987). "Boundary element methods in dynamic analysis." *Appl. Mech. Rev.* **40**(1), 1–23.

Bucker, H. P. (1979). "Propagation in a liquid layer lying over a liquid half-space (Pekeris cut)." *J. Acoust. Soc. Am.* **65**(4), 906–908.

Buckingham, M. J., and Giddens, E. M. (2006). "On the acoustic field in a Pekeris waveguide with attenuation in the bottom half-space." *J. Acoust. Soc. Am.* **119**(1), 123–142.

COMSOL AB (2020). COMSOL Multiphysics® v. 5.4, [www.comsol.com](http://www.comsol.com) (Last viewed 10-01-2021).

Dahl, P. H., and Dall'Osto, D. R. (2017). "On the underwater sound field from impact pile driving: Arrival structure, precursor arrivals, and energy streamlines." *J. Acoust. Soc. Am.* **142**(2), 1141–1155.

Deng, Q., Jiang, W., Tan, M., and Xing, J. (2016a). "Modeling of offshore pile driving noise using a semi-analytical variational formulation." *Appl. Acoust.* **104**, 85–100.

Deng, Q., Jiang, W., and Zhang, W. (2016b). "Theoretical investigation of the effects of the cushion on reducing underwater noise from offshore pile driving." *J. Acoust. Soc. Am.* **140**(4), 2780.

Ewing, W. M., Jardetzky, W. S., and Press, F. (1957). "Lamont geological observatory contribution," in *Elastic Waves in Layered Media* (McGraw-Hill, New York).

Fricke, M. B., and Rolfes, R. (2015). "Towards a complete physically based forecast model for underwater noise related to impact pile driving." *J. Acoust. Soc. Am.* **137**, 1564.

Hall, M. V. (2013). "A semi-analytical model for non-Mach peak pressure of underwater acoustic pulses from offshore pile driving." *Acoust. Aust.* **41**(1), 42–51.

Hall, M. V. (2015). "An analytical model for the underwater sound pressure waveforms radiated when an offshore pile is driven." *J. Acoust. Soc. Am.* **138**(2), 795–806.

Hastie, G., Merchant, N. D., Götz, T., Russell, D. J. F., Thompson, P., and Janik, V. M. (2019). "Effects of impulsive noise on marine mammals: Investigating range-dependent risk." *Ecol. Appl.* **29**(5), e01906.

Hazelwood, R. A., and Macey, P. C. (2016). "Modeling water motion near seismic waves propagating across a graded seabed, as generated by man-made impacts." *J. Mar. Sci. Eng.* **4**, 47.

Hazelwood, R. A., Macey, P. C., Robinson, S. P., and Wang, L. S. (2018). "Optimal transmission of interface vibration wavelets—a simulation of seabed seismic responses." *J. Mar. Sci. Eng.* **6**, 61.

Jensen, F. B., Kuperman, W. A., Porter, M. B., and Schmidt, H. (2011). *Computational Ocean Acoustics* (Springer, New York).

Kaplunov, J., Kossovich, L. Y., and Nolde, E. (1998). *Dynamics of Thin Walled Elastic Bodies* (Academic, New York), pp. 129–134.

Kim, H., Potty, G. R., Miller, J. H., Smith, K. B., and Dossot, G. (2012). "Long range propagation modeling of offshore wind turbine noise using finite element and parabolic equation models." *J. Acoust. Soc. Am.* **131**(4), 3392.

Lippert, S., Nijhof, M., Lippert, T., Wilkes, D., Gavrilov, A., Heitmann, K., Ruhnaud, M., von Estorff, O., Schäfer, A., Schäfer, I., Ehrlich, J., MacGillivray, A., Park, J., Seong, W., Ainslie, M. A., de Jong, C., Wood, M., Wang, L., and Theobald, P. (2016). "COMPILE—A generic benchmark case for predictions of marine pile-driving noise." *IEEE J. Oceanic Eng.* **41**(4), 1061–1071.

Lippert, T., Ainslie, M. A., and von Estorff, O. (2018). "Pile driving acoustics made simple: Damped cylindrical spreading model." *J. Acoust. Soc. Am.* **143**(1), 310.

Lippert, T., and Lippert, S. (2012). "Modeling of pile driving noise by means of wavenumber integration." *Acoust. Aust.* **40**(3), 178–182.

Lippert, T., and von Estorff, O. (2014). "The significance of parameter uncertainties for the prediction of offshore pile driving noise." *J. Acoust. Soc. Am.* **136**(5), 2463–2471.

MacGillivray, A. O. (2014). "Finite difference computational modeling of marine impact pile driving." *J. Acoust. Soc. Am.* **136**(4), 2206.

Marburg, S. (2002). "Six boundary elements per wavelength: Is that enough?" *J. Comput. Acoust.* **10**(01), 25–51.

Martin, S. B., and Barclay, D. R. (2019). "Determining the dependence of marine pile driving sound levels on strike energy, pile penetration, and propagation effects using a linear mixed model based on damped cylindrical spreading." *J. Acoust. Soc. Am.* **146**(1), 109.

McCullom, B. A., and Collis, J. M. (2014). "Root finding in the complex plane for seismo-acoustic propagation scenarios with green's function solutions." *J. Acoust. Soc. Am.* **136**(3), 1036.

Nealy, J. L., Collis, J. M., and Frank, S. D. (2016). "Normal mode solutions for seismo-acoustic propagation resulting from shear and combined wave point sources." *J. Acoust. Soc. Am.* **139**(4), EL95.

Press, F., and Ewing, M. (1950). "Propagation of explosive sound in a liquid layer overlying a semi-infinite elastic solid." *Geophysics* **15**(3), 426–446.

Reinhall, P. G., and Dahl, P. H. (2011). "Underwater Mach wave radiation from impact pile driving: Theory and observation." *J. Acoust. Soc. Am.* **130**(3), 1209–1216.

Rossington, K., Benson, T., Lepper, P., and Jones, D. (2013). "Eco-hydro-acoustic modeling and its use as an EIA tool." *Mar. Pollut. Bull.* **75**(1–2), 235–243.

- Schmidt, H., and Jensen, F. B. (1985). "A full-wave solution for propagation in multilayered viscoelastic media with application to Gaussian-beam reflection at fluid-solid interfaces," *J. Acoust. Soc. Am.* **77**(3), 813–825.
- Stickler, D. C. (1975). "Normal-mode program with both the discrete and branch line contributions," *J. Acoust. Soc. Am.* **57**(4), 856–861.
- Stöber, U., and Thomsen, F. (2019). "Effect of impact pile driving noise on marine mammals: A comparison of different noise exposure criteria," *J. Acoust. Soc. Am.* **145**(5), 3252.
- Tsouvalas, A. (2015). "Underwater noise generated by offshore pile driving," Ph.D. thesis, Delft University of Technology, Delft, Netherlands.
- Tsouvalas, A. (2020). "Underwater noise emission due to offshore pile installation: A review," *Energies* **13**(12), 3037.
- Tsouvalas, A., and Metrikine, A. V. (2013). "A semi-analytical model for the prediction of underwater noise from offshore pile driving," *J. Sound Vib.* **332**(13), 3232–3257.
- Tsouvalas, A., and Metrikine, A. V. (2014). "A three-dimensional vibroacoustic model for the prediction of underwater noise from offshore pile driving," *J. Sound Vib.* **333**(8), 2283–2311.
- Tsouvalas, A., and Metrikine, A. V. (2016). "Structure-borne wave radiation by impact and vibratory piling in offshore installations: From sound prediction to auditory damage," *J. Mar. Sci. Eng.* **4**(3), 44.
- Tsouvalas, A., van Dalen, K. N., and Metrikine, A. V. (2015). "The significance of the evanescent spectrum in structure-waveguide interaction problems," *J. Acoust. Soc. Am.* **138**(4), 2574–2588.
- Verfuß, T. (2014). *Noise Mitigation Systems and Low-Noise Installation Technologies* (Springer, Wiesbaden, Germany), pp. 181–191.
- von Pein, J., Klages, E., Lippert, S., and von Estorff, O. (2019). "A hybrid model for the 3D computation of pile driving noise," in OCEANS 2019 - Marseille, June 17–20, Marseille, France, pp. 1–6.
- Wilkes, D. R., and Gavrilov, A. N. (2017). "Sound radiation from impact-driven raked piles," *J. Acoust. Soc. Am.* **142**(1), 1.
- Wilkes, D. R., Gourlay, T. P., and Gavrilov, A. N. (2016). "Numerical modeling of radiated sound for impact pile driving in offshore environments," *IEEE J. Oceanic Eng.* **41**(4), 1072–1078.
- Zampolli, M., Nijhof, M. J., de Jong, C. A., Ainslie, M. A., Jansen, E. H., and Quesson, B. A. (2013). "Validation of finite element computations for the quantitative prediction of underwater noise from impact pile driving," *J. Acoust. Soc. Am.* **133**(1), 72–81.